

**Reliable Monitoring of Leak in Gas Pipelines Using
Acoustic Emission Method**

BY

HAZIM YALCINKAYA
B.S., Bogazici University, 2011

THESIS

Submitted as partial fulfillment of the requirements
for the degree of Master of Science in Civil Engineering
in the Graduate College of the
University of Illinois at Chicago, 2013

Chicago, Illinois

Defense Committee:

Dr. Didem Ozevin, Chair and Advisor
Dr. Michael J. McNallan, Civil and Materials Engineering
Dr. Craig D. Foster, Civil and Materials Engineering

TABLE OF CONTENTS

CHAPTER

1. INTRODUCTION.....	1
1.1. Statement of Problem.....	1
1.2. Objectives and Scope	2
1.3. Thesis Organization	3
2. BACKGROUND	5
2.1. Introduction.....	5
2.2. Pipeline Inspection and Monitoring Methodologies.....	5
2.3. Acoustic Emission Method for Leak Detection.....	9
2.3.1. AE Leak Characteristics	10
2.3.2. Leak Localization	12
2.4. Piezoelectric Phenomenon for Sensing.....	15
2.5. Calibration of Piezoelectric Sensors	18
3. LABORATORY SCALE LEAK DETECTION AND SENSOR SPACING IDENTIFICATION	20
3.1. Introduction.....	20
3.2. Experimental Design.....	20
3.2.1. Variables Affecting Leak Characteristics.....	23

TABLE OF CONTENTS (continued)

CHAPTER

3.2.2.	The Waveform Characteristics of Leak Source.....	24
3.2.3.	AE Amplitudes per Variable	27
3.2.4.	Leak Location Accuracy.....	31
3.3.	Numerical Model of the Pipeline Geometry.....	36
3.3.1.	Characteristics of Numerical Model.....	36
3.3.2.	Waveform Signatures and Attenuation Curve.....	38
3.4.	Discussion and Conclusion.....	44
4.	DESIGN MODELING AND CHARACTERIZATION OF PIEZOELECTRIC AE	
	TRANSDUCER.....	46
4.1.	Introduction.....	46
4.2.	Finite Element Models of Piezoelectric Transducer.....	47
4.2.1.	Transducer Design.....	47
4.2.2.	Multi-physics Model for Steel-Coupled Response.....	50
4.3.	Characterization Experiments.....	56
4.3.1.	Impedance and Bandwidth Measurement.....	56
4.3.2.	Transducer Response to Varying Input Source	58
4.3.3.	Directional Dependence with IR Laser-triggered Source.....	63
4.4.	Application on Leak Detection and Localization	67

TABLE OF CONTENTS (continued)

<u>CHAPTER</u>	
4.5.	Conclusion 71
5.	CONCLUSION 73
5.1.	Summary 73
5.2.	Findings..... 74
5.3.	Future Work 74
	CITED LITERATURE 76
	VITA 81

LIST OF TABLES

TABLE

I	Significant Cause Breakdown of Pipeline Failures, 2002-2011	2
II	Methods for Leak Detection.....	9
III	Variables Affecting Leak AE Characteristics	24
IV	Amplitude Levels at Channel 2 Divided by the Voltage for Fully Buried Orifice 1, 68.95 kPa.....	28
V	Mean and Standard Deviations for Unburied Pipe in cm	32
VI	Mean and Standard Deviations for Partially Buried Pipe in cm.....	33
VII	Mean and Standard Deviations for Fully Buried Pipe in cm	33
VIII	Mesh, Time Step and End Time of the Loading Function.....	38
IX	The Loss in dB/m for 10 kHz and 60 kHz Loading	44
X	The Properties of Two common PZT Ceramics Used for Sensing.....	48
XI	The Comparison of Leak Localization Ability of Cut-PZT and Normal-PZT for 1.27 mm Orifice Diameter	71

LIST OF FIGURES

FIGURE

1. Representative waveforms (a) Burst type (b) Continuous type	12
2. The orifices	21
3. A photograph of the pipeline with partially buried condition	21
4. Calibration curve of R6 obtained by ASTM E1106 (ASTM, 2007)	22
5. Leak waveform signatures (time versus voltage) for unburied, partially buried and fully buried cases (left to right) of (a) channel 1, (b) channel 2.	26
6. Leak waveform signatures (time versus voltage) for unburied, partially buried and fully buried cases (left to right) of (a) channel 1, (b) channel 2.	26
7. Leak waveform signatures (time versus voltage) for unburied, partially buried and fully buried.....	27
8. The frequency spectra of two AE sensors for the case of orifice 1, 68.95 kPa internal pressure and unburied pipe.....	30
9. The frequency spectra of two AE sensors for the case of orifice 3, 68.95 kPa internal pressure and unburied pipe.....	30
10. Leak location histogram example for unburied pipe.....	34
11. Leak location histogram example for partially buried pipe	34
12. Leak location histogram example for fully buried pipe	35
13. Leak localization error versus wave velocity	36
14. Finite element model showing the mesh density and the loading function for 60 kHz loading.	37

LIST OF FIGURES (continued)

FIGURE

15. Displacement histories for out of plane 60 kHz loading 0.8 m and 1.1 m away from the source.....	39
16. Displacement histories for out of plane 10 kHz loading 0.8 m and 1.1 m away from the source.....	40
17. Displacement histories for in plane 10 kHz loading 0.8 m and 1.1 m away from the source	41
18. Maximum amplitude values in r direction and exponential curve fit for 60 kHz	42
19. Attenuation Curve for 10 kHz loading in r direction	43
20. Attenuation Curve for 10 kHz loading in z direction	43
21. Geometric variables of piezoelectric transducer	48
22. Frequency domain model and the response history	50
23. Displacement around 60 kHz	52
24. Electric displacement field of normal-PZT	52
25. Finite element models on a pipe geometry coupled with cut-PZT and normal-PZT	53
26. Electrical potential histories for the 60 kHz load function in, (a) r direction, (b) z direction	54
27. Electric potential under 10 kHz loading.....	55
28. (a) Admittance results of three cut-PZT sensors, (b) the comparison of average result with the numerical model with 3% isotropic damping.....	56
29. The comparison of the transducer response to free boundary and coupled boundary to a steel plate.....	58

LIST OF FIGURES (continued)

FIGURE

30. Experimental setup to study the transducer linearity	59
31. Waveforms (with 40 dB gain) recorded from cut-PZT and normal-PZT under 8 V excitation in z direction.	59
32. Output response of cut-PZT and normal-PZT for the 400 μ sec window under varying input loading.....	61
33. Frequency sweep for the loading in r direction on pipe	62
34. Frequency sweep for the loading in z direction	62
35. The identification of transducer directivity with laser-based system.....	64
36. The waveform histories for 0°, 50° and 90° excitations; (a) cut-PZT,.....	65
37. The amplitude responses in radial direction; (a) cut-PZT, (b) normal-PZT	66
38. The frequency spectra for 0°, 50° and 90° excitations; (a) cut-PZT, (b) normal-PZT.....	67
39. Leak amplitudes of cut-PZT and normal-PZT transducers for different internal pressures	68
40. The source localization error with the sweep of wave velocity for cut-PZT and normal - PZT under 137.9 kPa and 344.7 kPa internal pressure	70

ACKNOWLEDGEMENTS

This research is supported by the National Science Foundation, Grant ECCS 1125114, entitled Preventing Imminent Failures of Pipeline Networks via Real Time Damage Detection and Location System. I would like to thank the organization for the necessary funding to complete the master of sciences degree. Also, I would like to thank my undergraduate advisors Dr. Kutay Orakcal, Dr. Gulay Altay, Dr. Gokmen Ergun, Dr. Ayhan Irfanoglu for their recommendation letters, which made my study in University of Illinois at Chicago possible.

I am very grateful to my research advisor Dr. Didem Ozevin for her generous time commitment and extraordinary patience. I was very lucky to have her as my graduate advisor. Many thanks to Aerielle Karr and Waltz Tsang for their help during the experiments. My labmates, Hossain Saboonchi and Zahra Heidary, Lu Zhang and James Bittner deserve special thanks for their help. I would like to thank my thesis committee members Dr. Michael J. McNallan and Dr. Craig D. Foster for being in my committee and their guidance.

SUMMARY

A steel pipe is built in the laboratory to study the variables affecting the leak source characteristics. The studied leak variables are internal pressure, leak size and earth pressure. The mechanical turbulence created by the leak is detected using piezoelectric transducers. The amplitude output of the piezoelectric transducer versus internal pressure curves are plotted for different earth conditions to study buried and on-ground pipelines. A numerical model is then created to find the attenuation factors on the pipe geometry for a specific loading frequency. The required transducer spacing is determined for a specific frequency on an unburied pipe. Leak localization accuracy is also studied on the same pipe geometry. The leak localization results for each case are shown in tables, and the histograms show how the leak localization accuracy changes with the earth pressure.

A new shear mode acoustic emission transducer is designed for pipeline leak detection applications with the intention of increasing the spatial locations of the transducers. Numerical modeling of the transducer for frequency design is shown and compared with the experimental results. The amplitude of the shear mode sensor is compared with the normal mode sensor output numerically and experimentally. The ultrasonic transducer is used to generate sine waves on the pipeline geometry in normal and tangential directions to demonstrate their difference in polarization directions. Leak localization results are also compared between two transducers. The angular dependence of shear mode and normal mode sensors to a controlled source created by Q-switched Nd:Yag laser is plotted in polar coordinates, which can be used for the absolute calibration of the AE transducers.

CHAPTER 1

INTRODUCTION

1.1. Statement of Problem

Among civil infrastructures, pipeline networks are the lifeline infrastructures of the world in order to transmit gas, oil, water and steam from one location to another. As they carry environmentally hazardous materials (e.g. gas, oil) and valuable products (e.g. water), their losses due to structural failures and leakage are risky and negatively affect the environment and human lives. Pipeline and Hazardous Material Association (PHMSA, 2012) reported property damages of about \$450 millions, 16 fatalities and 61 injuries as the annual average between 2002 and 2011. Moreover, a yearly average of 110,963 gross barrels of hazardous fluid is spilled between 2002 and 2011. Table I summarizes the main causes of the pipeline failures. For gas transmission pipelines, corrosion-related damages make up 22.7% of the total damages. Excavation damages, corrosion and material failures are the leading causes for pipeline failure. With the monitoring of the buried and on ground pipelines, these damages could be discovered before causing catastrophic failure or significant damage. The NTSB report (Douglass, 2009) concludes that “Current inspection and testing programs are not sufficiently reliable to identify features associated with longitudinal seam failures of ERW pipe prior to catastrophic failure in operating pipelines.” Caley et al. (Caley et al., 2008) demonstrated that prioritizing pipeline inspection and maintenance based on failure data might establish incorrect prioritization due to significant uncertainty of pooling failures of dissimilar pipeline systems data. If the damage is

diagnosed early, it can be repaired, and the pipeline can be functional in a short period of time without any adverse impact on the society.

TABLE I
Significant Cause Breakdown of Pipeline Failures, 2002-2011

Percentage	Causes
18.5%	Corrosion
23.5%	Excavation Damage
6.5%	Incorrect Operation
18.4%	Material/Weld/Equipment Failure
7.9%	Natural Force Damage
5.4%	Other Outside Force Damage
19.8%	All Other Causes

1.2. Objectives and Scope

The detection of leaks for oil, water or natural gas pipelines before reaching structural instability is important to prevent any catastrophic failure, and consequently, detrimental environmental impact. The Acoustic Emission (AE) method is a nondestructive testing method that relies on propagating elastic waves generated by damage initiation or any other external stimulus such as impact. As compared to vibration based methods, typical operational frequency of the AE method is above 20 kHz (audible frequency). When a structure is under loading, a

crack or leak may initiate and generate propagating elastic waves. AE sensors (e.g. piezoelectric contact sensors) detect the surface motion. Using an array of sensors, the leak source can be located in 1D, 2D or 3D depending on number of sensors and geometry. The AE method is capable of source localization by means of local, global, remote and online monitoring. However, the attenuation in the pipe structure requires densely populated sensor arrays for leak localization, which limits the applicability of the method for long range pipeline networks.

The main objectives of this research are to understand the leak characteristics under varying pipe conditions and to study different geometry piezoelectric sensors for increasing the spatial distribution of sensors. A laboratory scale pipeline is built, and the leak rate is varied through leak size and internal pressure. After understanding the leak characteristics, the new piezoelectric sensors at 60 kHz are designed and compared with conventional piezoelectric sensors. The attenuation characteristics, the sensor frequency domain response and the structural coupled response of the sensors are studied using a multi-physics finite element models. Based on the outcomes of the experimental and numerical data, improvements in leak detection and localization are presented.

1.3. Thesis Organization

Chapter 2 presents the literature review implemented in this research including pipeline leak detection methodologies, acoustic emission methods specific for pipeline leak detection and localization, and the piezoelectric phenomena for sensing elastic waves. Chapter 3 presents the results of experimental scale pipeline tests for understanding the leak characteristics. The error of leak localization with conventional AE sensors is shown, and the attenuation factors for two frequencies are found numerically to identify the required spacing between the sensors. Chapter

4 explains the design of a new in-plane sensitive piezoelectric sensor in order to increase the sensor spacing further than the conventional piezoelectric sensor. The electromechanical characterization tests are compared with the numerical frequency domain analysis. The new sensor performance to detect and locate leak is compared with that of the conventional piezoelectric sensors. Finally, Chapter 5 discusses the overall results of the research and future work.

CHAPTER 2

BACKGROUND

2.1. Introduction

In this chapter, the fundamental background utilized in this research is summarized. First, pipeline inspection and monitoring methodologies are presented. The application of acoustic emission method for leak detection and localization is discussed together with the limitations. The theory of piezoelectricity that is presented is implemented for designing the shear type AE sensors for long-range leak detection. The literature on the AE sensor calibration approaches is discussed.

2.2. Pipeline Inspection and Monitoring Methodologies

Leaks occur in pipelines due to corrosion (Ahammed and Melcher, 1995), insufficient welding (Yaorong et al., 2001), excavation, incorrect operation, natural force damage and equipment failure. Yaorong et al. (Yaorong et al., 2001) performed a fitness for service (FFS) assessment of pipelines. The main failure reason for oil pipelines is stated as the “lack of fusion defects formed by inadequate welding heat input in electric resistance welded (ERW) pipe welds.” Variation in the internal pressure of a pipe increases the risk of defect scattering along the pipeline. Typical inspection methods include radiography and ultrasonics. Carvalho et al.

(Carvalho et al., 2008) compares the effectiveness of radiography, manual and automatic ultrasonic techniques using pulse-echo, and automatic ultrasonic techniques by time of flight diffraction. It is concluded that the automatic ultrasonic technique is better than other techniques since it shortens the time required to perform the test and have a higher probability for detection.

Some inspection methods require the pipeline to be shut down for damage detection. For instance, Kishawy and Gabbar (Kishawy and Gabbar, 2010) expressed the need for hydrostatic testing to detect the axial flaws on pipelines. The hydrostatic test is a strength test that is performed before the pipelines are used. The fluid carried by the pipeline should be removed before the hydrostatic test. Researchers also mentioned smart pigs which can be used for the inspection of liquid transmitting pipelines either by detecting metal loss or crack along the pipe. Gloria et al. (Gloria et al., 2009) developed an internal corrosion sensor, which evaluates the change in the pattern of magnetic flux, similar to smart pigs, to detect metal loss, which causes the reduction of pipe wall thickness. This sensor is superior to conventional smart pigs because it can be used in pipes with smaller wall thickness as it does not exploit the magnetic saturation of the pipe wall.

In addition to intermediate inspection approaches, there are several pipeline leak detection methodologies in the literature for real time leak detection and localization. The selection of the monitoring method depends on the material being transmitted such as gas or liquid. Leak detection methods can be categorized as internal methods and external methods depending on the utilization of the internal or external parameters of the pipeline for leak detection. El-Sheikh (El-Sheikh, 2010) described mass balance, pressure drop as internal methods and cable sensors, liquid sensing and vapor sensing as external methods for leak detection. Cable sensors work on the principle that the leakage causes short circuit in the electric

current flow which makes an alarm sound. It only works for non-conductive fluid transportation. Liquid sensing is the method in which liquid sensing cables are placed adjacent to pipelines to transport lower energy to the recording unit when a leak occurs due to the increase in the impedance of cables. Hence, presence of lower energy indicates the leak. Vapor sensing is the method where the soil samples taken around the pipeline are analyzed for contamination by the oil transported.

Billman and Isermann (Billman and Isermann, 1987) described typical gas and liquid leak detection methods as balancing, shockwave base methods, fault model filters, and fault sensitive filters. Inlet pipeline pressures and outlet flow rates are monitored with different sampling frequencies and different nodes along the pipe for gases and liquids pipelines as liquid flow velocity is higher than gas flow velocity. Stouffs and Giot (Stouffs and Giot, 1993) examined the leak detection threshold for liquid pipelines using outlet flow rate. The authors claim that the accuracy of mass flow rate measurement device is the only factor affecting the leak detection threshold during steady state flow. During transient flow, the time interval at which mass balance is computed and roughness of transient flow are the two factors affecting the leak detection threshold. Kam (Kam, 2010) used inlet pressure and outlet flow rate monitoring to detect leakage on subsea pipelines carrying oil in both gas and liquid states. This research shows that leak detection is more accurate when the orifice size is greater, and when the location of leak is closer to upstream and backpressure is lower.

Ground Penetrating Radar (GPR) is the geophysical method to survey the landscape. These devices give images of the subsurfaces and features of the soil. Also geological applications on this device can be used to detect the rebar locations and inspect buried pipelines. Hyun et al. (Hyun et al., 2007) built a GPR system, which is utilized for leak detection on a

laboratory scale buried pipe carrying water. Ground removal and neighboring differences can mask the detection of the leak so the effects of those variables are reduced selecting the B-scan approach of ground penetration radar. To see the leak clearly, diffraction tomography is further applied on the scanned images.

Among monitoring methods, the Acoustic Emission (AE) method has an advantage of pinpointing the leak location in a real time testing. The comparison of the AE method to other leak inspection and monitoring methods is summarized in Table II. The disadvantage of the AE method-the close proximity of sensors due to attenuation in pipeline structures- is studied in this research in order to increase the sensor spacing with unique geometric sensor design and the laboratory scale understanding of leak characteristics. The details of the AE method are described in the next section.

TABLE II
Methods for Leak Detection

Method	Advantages	Disadvantages
Acoustic Emission	Detecting small leaks unburied/buried pipes and localization in 1D, 2D or 3D	Close sensor spacing necessary due to attenuation, noise influence
Cable Sensors	Continuous sensors to pinpoint leak accurately	Insulation is required when conductive material is being transported
Liquid Sensing	Accurate leak detection	Expensive
Vapor Soil	Independent from operator experience	Limited for buried pipelines and leak penetration, sampling
Ground Penetrating Radar	Effective for buried pipelines	Expensive and limited for buried pipelines and depth
Mass Balance	Inexpensive and easy to implement	Longer monitoring period and inaccurate
Pressure Drop Method	Applicable to subsea applications	Insensitive to leaks smaller than 1% of flow rate
Radiography	Sensitive to microcracks	Radiation damage to operator
Ultrasonics	Easy operation	The requirement of experienced operator and accessibility

2.3. Acoustic Emission Method for Leak Detection

ASTM E1316 (ASTM, 2011) defines acoustic emission (AE) as “the class of phenomena whereby transient stress/displacement waves are generated by the rapid release of energy from localized source within a material, or the transient waves so generated.” The AE method is a passive non-destructive testing method that relies on the propagating elastic waves released from active sources. Examples of sources that generate AE activities include crack growth, mechanical

friction and leaks, which have two characteristic waveform signatures; burst type and continuous type. In addition to typical pipeline integrity management approaches such as the mass-balance method and the pressure drop method (Kishawy and Gabbar, 2010), AE has been studied by several researchers since 1980s. As compared to the acoustic noise based approach (Fuchs and Riehle, 1991) through monitoring frequencies less than 400 Hz, a typical application of the AE method relies on propagating elastic waves through pipe structure in the frequency range of 1 kHz – 60 kHz. Kupperman et al. (Kupperman et al., 1985) demonstrated that the leak detection in reactor components with acoustic emission has the minimum leak rate as 0.23 liter/hour in laboratory environment; however, the threshold to detect the leak rate depends on the pipe geometry, material, internal pressure and measurement system selected. Miller et al. (Miller et al., 1999) designed a reference standard pipe to evaluate the AE equipment for leak detection.

2.3.1. AE Leak Characteristics

The leak source causes continuous emission which is defined by ASTM E 1316 (ASTM, 2011) as “a qualitative description of the sustained signal level produced by rapidly occurring acoustic emission sources”. The detection approach and data processing of continuous emissions are different from burst emissions because of the indefinite arrival time and end time of elastic waves.

Ozevin and Harding (Ozevin and Harding, 2012) explained the equations for the burst type and continuous type AE signals as follows

$$V_{Burst} = V_0 \sin(2\pi f_0 t) \{ (1 - e^{-(t-t_{arrival})/t_{rise}}) \in [0, 1] \times e^{-(t-t_{arrival})/t_{decay}} H[t - t_{arrival}] \} \quad (2.1)$$

$$V_{continuous}(t) = \sin(2\pi f_0 t) \sum_{i=1}^{\infty} V_i \{(1 - e^{-(t-t_{arrival})/t_{rise}}) \in 0...1\} \times e^{-(t-t_{arrival}(i))/t_{decay}(i)} H[t - t_{arrival}(i)] \quad (2.2)$$

where V is the amplitude, f_0 is the frequency, $t_{arrival}$ is the arrival time, t_{decay} is the decay time and H is the Heaviside step function.

Both signals are sinusoidal waves decaying exponentially; however, burst type signals have only one term clearly describing the rise time and decay time of the signal. The continuous wave is a summation of multiple waves with the same or different frequency but with a different rise, arrival and decay time. Crack growths and leaks are examples of burst and continuous type waveforms, respectively. Due to indefinite arrival time of continuous emissions, leak localization becomes a challenging task. Figure 1 shows examples of burst and continuous type representative waveforms obtained from equations 2.1 and 2.2. These waveforms are created for 50 kHz frequency. The single waveform for the burst type has decay time of 6.36×10^{-5} seconds. For the continuous type, three waveforms are plotted below with 50 kHz, different amplitudes, and different arrival and decay times.

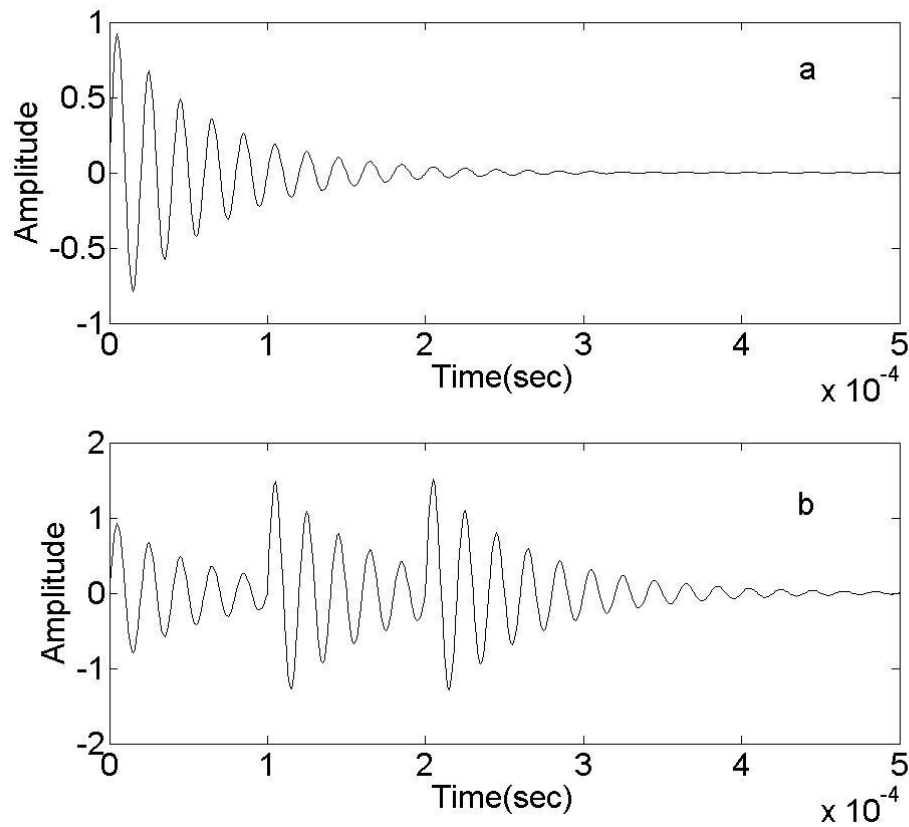


Figure 1. Representative waveforms (a) Burst type (b) Continuous type

2.3.2. Leak Localization

The fundamental advantage of the AE method is the capability to pinpoint the leak location in real time. Leak localization with the AE method depends on the intensity of the leak source and the attenuation factors affecting the propagating waves on the pipe material. However, the waveforms become modified upon propagating from the initiation point to the sensors because of the reflections at the interfaces and the inhomogeneities on the path taken (Wood and Harris,

2000). Another source of error is the attenuation and the dispersion of the waveform which refers to the change of wave velocity because of the frequency and the thickness of the medium.

Grabec (Grabec, 1978) developed leak localization using the cross correlation technique, which has limited success due to the influence of reflected waves and multiple wave modes. There are many studies since then to improve the location accuracy of continuous emissions. For instance, Hessel et al. (Hessel et al., 1996) applied the neural network approach to improve the leak detection with airborne sensors, though the approach may not be applicable to different pipeline configurations. Grabec et al. (Grabec et al., 1998) applied a neural network through the usage of the prototype waveform signatures on contact transducers to overcome the limitations of cross correlation function. The same research group improved the arrival time determination with applying a certain digital filter to AE waveforms before the cross correlation function (Hessel et al., 1996). Gao et al. (Gao et al., 2004) also studied the effect of filtering on leak detection in plastic water pipelines. Fukuda and Mitsuoka (Fukuda and Mitsuoka, 1986) applied pre-whitening filter to AE waveforms to improve the leak detection and location through identifying a definite peak as the result of cross correlation of two waveforms. Wavelet transformation is implemented to analyze complex leak signatures (Ahadi and Bakhtiar, 2010). Jiao et al. (Jiao et al., 2004) used the dispersion curves of pipelines to identify the leak location with a single sensor even though the waveform can still be influenced with reflections and multiple-sources in a realistic test.

Background noise is a major problem for the AE method. Kalyanasundaram et al. (Kalyanasundaram et al., 1989) encountered the same problem while trying to locate both water and air leakage on a Pressurized Heavy Water Reactor. The leak location determination in time domain was not successful because of the high background noise masking the pressure waves

generated due to the leakage. Hence, the leak localization was done in a frequency domain and found that the frequency of AE signal depends on the “size, shape and morphology of the crack”.

In order to increase the sensor spacing with an acceptable range, the AE sensors used for locating the leak in pipelines are selected to have low resonance frequency (<80 kHz). Miller et al. (Miller et al., 1999) did the field test for leak localization with a 15 kHz resonant sensor. Different amplitude levels are recorded for different pressure levels and the types of leakage, turbulent or non-turbulent. For a better leak location result, the sensors have different threshold levels. The author defined this method as tuning, the “adjustment of system threshold to produce an optimum hit rate on each channel.”

For any leak localization method, the dispersion (wave mode and frequency dependent velocity) and attenuation limit the minimum detectable leak rate and the maximum sensor spacing (Beck et al., 2005). Muggleton et al. (Muggleton et al., 2004a) studied wave attenuation in plastic water pipes for frequencies less than 1 kHz. The attenuation factor depends on pipe material and geometry, surrounding medium and internal medium. Leak detection and location are more challenging in gas pipelines than water pipelines because of the smaller particle sizes of gas compared to water, which is the main source of AE through creating turbulence events at the leak location. Further, the signal decays with a higher rate and lose energy due to the pressure caused by the buried pipelines as compared to on-ground pipelines or submerged pipelines (Muggleton et al., 2004b). The reliable leak detection using the AE method requires understanding leak waveform characteristics as a function of pipe operational conditions and estimating the signal attenuation to define the discrete sensor spacing for pinpointing leak position spatially.

2.4. Piezoelectric Phenomenon for Sensing

Piezoelectric effects are categorized as direct effects (sensing) or converse effects (actuating). Direct effect is the occurrence of polarization when the stress is applied to the material. Converse effect is the opposite of the direct effect. When electric field is applied to a piezoelectric material, the vibration of piezoelectric element causes stress on the surface on which it is mounted. The actuation and sensing equations provided by IEEE standard 176 (IEEE, 1987) are as follows

Actuation Equations:

$$S_{ij} = s_{ijkl}^E T_{kl} + d_{kij} E_k \quad (2.3)$$

$$D_i = d_{ikl} T_{kl} + \varepsilon_{ik}^T E_k \quad (2.4)$$

Sensing Equations:

$$S_{ij} = s_{ijkl}^D T_{kl} + g_{kij} D_k \quad (2.5)$$

$$E_i = g_{ikl} T_{kl} + \beta_{ik}^T D_k \quad (2.6)$$

where T is the stress tensor, E is the electric field, d is the piezoelectric charge constant, D is the electric displacement field or polarization, S is the strain field, g is the piezoelectric voltage coefficient, ε is the dielectric permittivity, the superscript D and T denotes the electric displacement field is constant and the stress is constant, respectively.

Giurgiutiu (Giurgiutiu, 2008) added temperature terms to the equations 2.3-2.6. These terms are the result of pyroelectricity in piezoelectric materials. Pyroelectricity is the electrical

field generation in the material because of the temperature change. Some pyroelectric materials have the properties of ferroelectric materials. Tichy et al. (Tichy et al., 2010) defined the ferroelectricity as “a polar material, whose electric dipoles can reverse direction as a consequence of an external electric field.” Kholkin et al. (Kholkin et al., 2008) expressed that ferroelectric materials have higher piezoelectric coefficients. The ferroelectric materials lose their piezoelectric properties above a certain temperature called the Curie temperature, but the materials’ piezoelectric coefficients increase as the material is approaching this temperature. Tichy et al. (Tichy et al., 2010) used lead zirconate titanate as the example of the advancement in the piezoelectric technology and indicated that for optimum results, these materials are designed to vibrate at their resonant frequencies. The piezoelectric material can be also permanently polarized in a direction for a better voltage output.

Electromechanical coupling coefficient is another important piezoelectric property. It shows the efficiency of the material to convert electrical energy into mechanical energy or vice versa. Electromechanical coupling coefficient k is the square root of mechanical energy stored over electrical energy applied, and is a unitless quantity, provided in equation 2.7 (Giurgiutiu, 2008). If k reaches one, this indicates that the piezoelectric material functions better at the selected direction of motion and the energy loss is at the minimum.

$$k = \sqrt{\frac{E_{Mechanical}}{E_{Electrical}}} \quad (2.7)$$

IEEE standard 176 (IEEE, 1987) presents the cuts or rotations and corresponding notations for single, double and triple rotated plates, which can be utilized to achieve higher piezoelectric coefficients in the desired direction. Additionally, the standard shows the excitation modes to exploit for the sensor applications. These modes are thickness excitation of thickness vibrations, lateral excitation of thickness vibrations, low-frequency extensional vibrations of rods, and radial modes in thin plates. The mode of vibration can be chosen based on the piezoelectric coefficients d_{12} , d_{13} , d_{14} , d_{21} , d_{23} , d_{25} , d_{31} , d_{32} , d_{36} . For sensing characteristics of piezoelectric materials, the piezoelectric voltage coefficient g needs to be maximized.

The most common transduction principle to detect acoustic emissions is piezoelectricity. The electrical and mechanical properties of piezoelectric transducers depend on the material, structural shape and size. The most common piezoelectric material for acoustic emission sensing is lead zirconate titanate (PZT), which has a high quality factor and resonant behavior. Proctor (Proctor, 1982) developed a piezoelectric transducer which consists of a conical active element made of PZT and an extended backing with a wideband frequency response. However, this transducer is not applicable for field testing due to its size and geometry. Sause et al. (Sause et al., 2012) studied the finite element models of conical transducer coupled to different medium. Proctor (Proctor, 1988) also designed tangential AE (shear mode) transducer through polarizing the ceramic parallel to electrodes. The transducer sensitivity is 0.3-0.5 mV/pm with the vertical mode rejection as 30 dB less than the tangential mode. Lee and Kuo (Lee and Kuo, 2001) miniaturized the conical active element of this transducer using the excimer laser technique. Or et al. (Or et al., 2000) studied the polyvinylidene fluoride/trifluoro ethylene (P(VDF-TrFE)) copolymer as an acoustic emission sensor. Marin-Franch et al. (Marin-Franch et al., 2002) tested PTCa/PEKK piezo-composites for surface mounting and embedding of AE sensors.

2.5. Calibration of Piezoelectric Sensors

The AE sensor calibration (input-output relationship) is needed for quantitative AE analysis. ASTM E1106 (ASTM, 2007) describes the method for absolute calibration of AE sensors. This calibration method uses breakage of glass capillary as a mechanical source. This mechanical source generates a force step function on a steel block. Two transducers (i.e. transducer under test and standard transducer) are mounted on the same surface where the breakage is performed. The surface waves generated are captured by two sensors which are sensitive to normal displacement. The calibration is performed relative to the standard transducer in a frequency domain with units of V/m, V/m/s or V/m/s² depending on the response of sensor. The calibration approach requires a finely polished steel cylinder with the dimensions sufficiently large to prevent any reflections during the duration of surface wave arrival.

Hatano et al. (Hatano et al., 1998) developed the reciprocity calibration. The transducers are arranged on a steel block differently for the Rayleigh wave and longitudinal wave calibration. Squared sine shape wave bursts from 100 kHz to 2 MHz with 5 kHz increments are generated by one sensor, and the propagating waves are received by the other sensor and a calibration curve is plotted in the frequency domain. The method assumes that the sensors behave exactly the same as the actuation and passive modes. McLaskey and Glaser (McLaskey and Glaser 2012) discusses that the method does not function for the sensors with the built-in preamplifier.

Theobald et al. (Theobald et al., 2005) did the calibration for out-of-plane displacement on a glass block using one transducer for sine wave generation and another transducer for the reception. Interferometer is used for recording the absolute normal displacement. The voltage

generated by the sensor is divided by the displacement detected using the interferometer to obtain a V/m curve in the frequency domain.

Theobald (Theobald, 2009) introduced calibration for in-plane displacements. A shear wave transducer as a source is mounted on a half aluminum sphere, and in-plane displacement is recorded with an interferometer in a horizontal position. An AE transducer used in receptive mode is more sensitive to out-of-plane displacements. The calibration of the in-plane direction is performed through distinguishing shear wave from compression wave with the arrival times.

McLaskey and Glaser (McLaskey and Glaser, 2012) used the ball impact and glass capillary fracture as the source function for the sensor calibration. The displacements created by these sources at the transducer positions are modeled analytically with the Green's functions, and sensors are calibrated relative to this displacement values in the frequency domain.

None of these studies discussed above consider the bulk characteristics of the piezoelectric sensor that is critical for converting the waves into electrical signal at different directions. Therefore, there is a need for calibration method considering the sensitivity of the transducers in all directions.

CHAPTER 3

LABORATORY SCALE LEAK DETECTION AND SENSOR SPACING

IDENTIFICATION

3.1. Introduction

In this study pipeline geometry similar to the ones used in gas distribution networks is built in laboratory. The pipeline conditions including internal pressure, leak size and surrounding earth pressure are varied in order to identify the AE leak characteristics. A longer pipeline model is built numerically under dynamic loading in order to identify the attenuation characteristics of particular geometry and frequency (10 kHz and 60 kHz selected). Based on the experimental AE amplitude and numerical attenuation curve, the sensor spacing for reliable leak detection and location is identified.

3.2. Experimental Design

A 152 cm long, 11.43 cm diameter steel pipeline is built in the laboratory to be tested for leak generation at different operational conditions including the internal pressure level created through air (68.95 kPa to 344.74 kPa with 68.95 kPa increments) and the presence of earth pressure (unburied, partially buried and fully buried cases). The pipe is a steel pipeline which is welded with a cap at one end to stop the air flow. The other end is connected to air inlet through a hose. To make sure the air is coming out only from the leak hole, a valve is placed 17 cm away from the end. The leak hole is varied through three different orifice diameters as 0.41 mm, 0.64 mm and 1.3 mm. The orifice is mounted through the pipe thickness through threaded bolts, similar to the design of Miller et al. (Miller et al., 1999). The pipe is built in a wooden box which

has two holes to slide the pipe through and an open top so that pipe can be covered with soil. Figure 2 shows the three orifices that were used during experiments and Figure 3 shows the experimental setup when the orifice is buried with soil. Two AE sensors are placed to two sides of the leak point. The sensors used in this study are R6 sensors, which have resonance at 60 kHz with the operating frequency of 35-100 kHz. For the fully buried case, the AE sensor 1 is also buried into the soil to investigate the effect of earth pressure on the sensor response. The R6 sensor 1 and sensor 2 are located 76.2 cm and 45.7 cm away from the leak source, respectively.

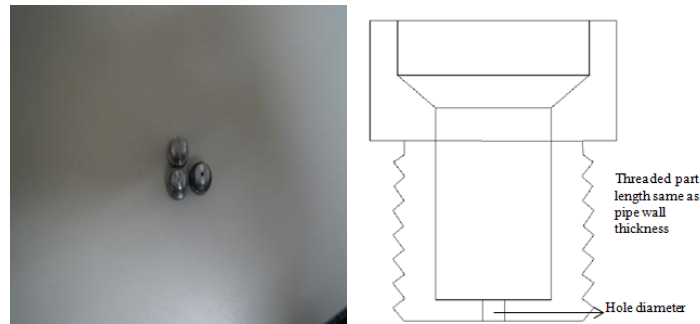


Figure 2. The orifice sizes and the design



Figure 3. A photograph of the pipeline with partially buried condition

Figure 4 shows the calibration curve of R6 provided by the manufacturer. The calibration curve is obtained by ASTM E1106 (ASTM, 2007). The sensor response is amplified when loading is around 60 kHz frequency. As the output signal is linearly proportional to the stress tensor, numerically obtained attenuation curves can be linked with the experimental response in order to estimate the maximum sensor spacing for the target leak rate and the pipeline operational condition.

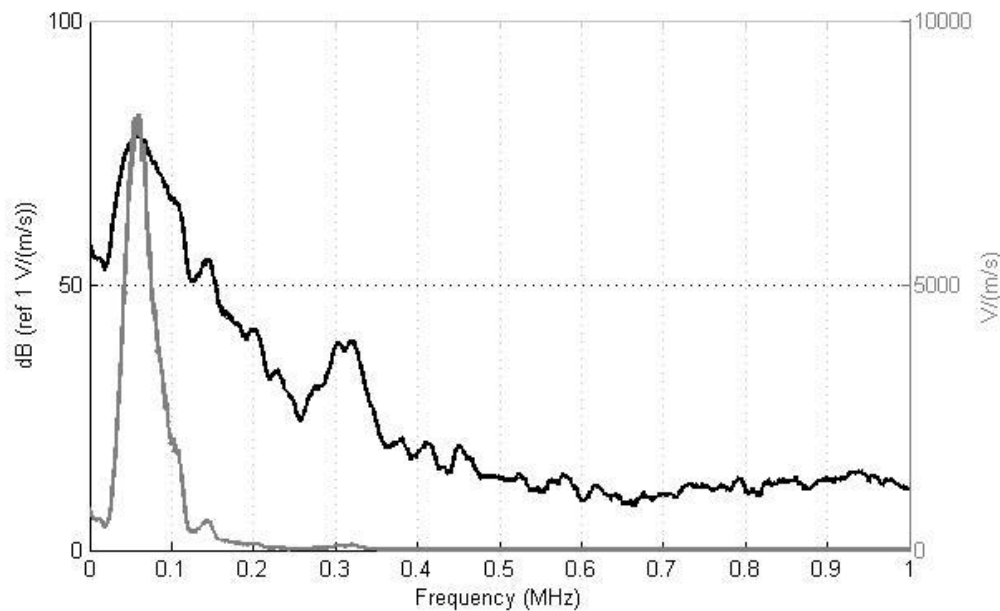


Figure 4. Calibration curve of R6 obtained by ASTM E1106 (ASTM, 2007)

3.2.1. Variables Affecting Leak Characteristics

Experimental variables affecting leak characteristics are leak size, internal pressure and earth pressure. Leak size is changed by inserting orifices with different diameters into the thickness of the steel pipe. As the orifice diameter increases, the leak rate increases. The increase in leak size results in a more chaotic behavior at the leak location. This is proven by the amplitude increase in the sensors' responses. Another important finding is the frequency shift when the leak size is changed. When the leak size is increased, there is a decrease in the frequency content as described in the next part.

Internal pressure in the pipe is increased via air up to 344.74 kPa, and sensor response is recorded for every 68.95 kPa pressure decrease. The decrease in internal pressure also reduces the leak rate. Hence, internal pressure decrease also means decrease in sensor response.

The test is repeated for three cases: unburied, partially buried and whole buried pipes. The section of the pipe with the length of 55.9 cm is buried with soil and gravel mixture including the orifice location. This condition is referred to as the partially buried condition. The fully buried case is defined as the condition that the complete pipe within the box is buried with soil and gravel mixture. In this condition, one of the AE sensors is also covered with the soil. The height of the soil layer is 12.7 cm from the top surface of the pipe.

Table III summarizes the experimental variables, ranges and their effects on AE leak characteristics. The details of the effects of three variables on leak characteristics are discussed in detail below. In summary, the most challenging case for leak detection is the minimum internal pressure and orifice size with the fully buried condition. Based on the operational

condition of pipe and the acceptable leak size, the reliable leak detection using AE method with the selected sensor spacing can be identified.

TABLE III
Variables affecting leak AE characteristics

Variable	Value Range	Effect on Leak Characteristics
Pipe internal pressure	$P_{\text{initial}} = 68.95 \text{ kPa}$	Increase in chaotic turbulence flow around the leak location
	$P_{\text{end}} = 344.74 \text{ kPa}$	
	$\Delta P = 68.95 \text{ kPa}$	
Orifice size	0.41 mm	Increase in amplitude and decrease in frequency content with the increase of orifice diameter
	0.64 mm	
	1.27 mm	
Earth pressure	Unburied	Decrease in propagating wave amplitude due to additional boundary constraint caused by the earth pressure
	Partially buried	
	Fully buried	

3.2.2. The Waveform Characteristics of Leak Source

Two different modes are available for AE waveform recording in the data acquisition system used in this study (PCI-8 board manufactured by Mistras Group Inc): AE mode and TRA mode. AE mode is the conventional threshold based approach to detect initiation of leak waveforms. In TRA mode, the AE sensors are synchronized; in other words, if one channel is triggered, the data acquisition system records AE signals from all of the active channels. Continuous waveforms do not have a well defined signal arrival as shown in previous chapter.

Therefore, data acquisition in AE mode may cause incorrect channel sequence for localization. In this study, TRA mode is used for recording leak waveforms. With this setup, it is ensured that the closest sensor to the leak source triggers all the active AE channels as it is expected that the nearest sensor would have the highest amplitude.

Figure 5 shows the waveforms detected for three conditions as unburied, partially buried and fully buried conditions for channels 1 and 2, respectively. The orifice diameter and internal pressure are 0.41 mm and 206.84 kPa. The presence of earth pressure around the orifice or the leak location causes significant loss of amplitude as the soil reduces the impact energy that the leak turbulence causes. For the fully buried case, channel 1 is also buried and there is no influence of earth pressure on the sensor response. For this orifice size, there is no significant effect for the fully pipe buried case as compared to the partially buried case. However, when the orifice size increases, the effects become apparent as shown in Figure 6. These plots show the waveforms for 1.27 mm orifice with 206.84 kPa internal pressure. The highest amplitudes are obtained for the unburied case while the lowest amplitudes are obtained for the fully buried case.

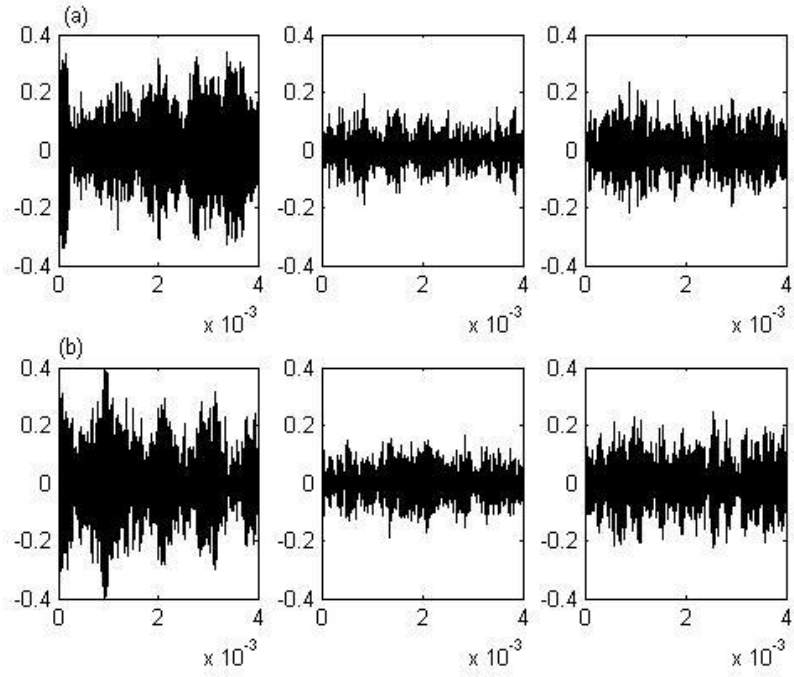


Figure 5. Leak waveform signatures (time versus voltage) for unburied, partially buried and fully buried cases (left to right) of (a) channel 1, (b) channel 2.

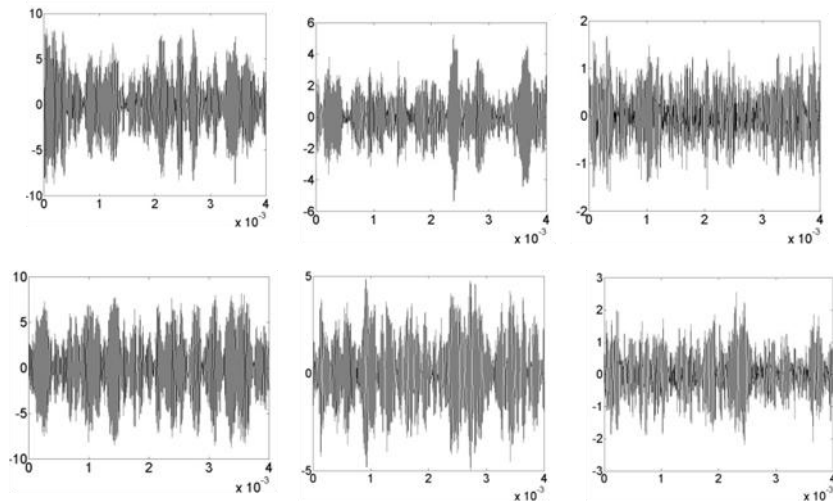


Figure 6. Leak waveform signatures (time versus voltage) for unburied, partially buried and fully buried cases (left to right) of (a) channel 1, (b) channel 2.

3.2.3. AE Amplitudes per Variable

The AE amplitudes for different leak conditions are presented in Figure 7. The AE amplitude increases as the internal pressure increases. For the unburied case, the amplitude does not vary much after 200 kPa as the AE system reaches its maximum dynamic range. There is a slight difference in the responses of two sensors as there is about a 3 dB difference in the sensitivity that reflects into the output signal. When the leak size or the orifice size increases, the AE amplitude increases as well. When the pressure increases, the turbulence at the leak location increases and causes more chaotic behavior and higher impacts, and as a consequence, higher amplitude elastic waves, which agrees with the result of Yang et al. (Yang et al., 2007). There is an exception for the fully buried case that the AE amplitudes of orifices 2 and 3 indicate similar trends with pressure changes.

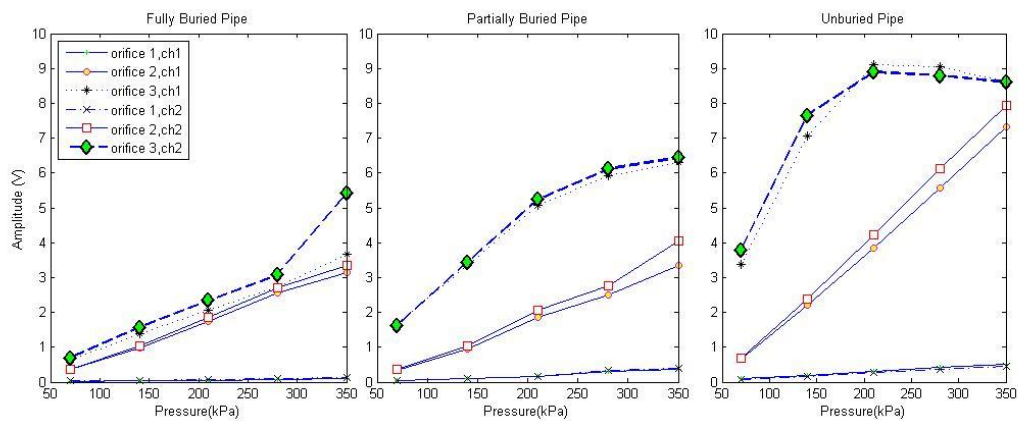


Figure 7. Leak waveform signatures (time versus voltage) for fully buried, partially buried and unburied pipes

TABLE IV

Amplitude Levels at Channel 2 Divided by the Voltage for Fully Buried Orifice 1, 68.95 kPa

Orifice	Pressure(kPa)	Unburied Reading	Partially Buried Reading	Fully Buried Reading
0.41 mm	68.95	2.7	1.7	1
	137.9	5.4	3.1	1.5
	206.85	8.7	5.6	2
	275.8	12.1	10.6	2.9
	344.75	15	13.1	3.9
0.64 mm	68.95	22.6	12.2	12
	137.9	77.7	33.2	33.7
	206.85	136.6	66.5	59.9
	275.8	198.9	89.3	87.3
	344.75	257.7	131.6	108.5
1.27 mm	68.95	122.8	52.7	22.6
	137.9	247.8	111.5	51.1
	206.85	288.1	169.9	75.9
	275.8	285.2	198.4	99.6
	344.75	278.9	208.9	175.4

Table IV above shows the AE amplitude changes with the pressure, orifice size and external pressure. The test condition case with the 0.41 mm orifice diameter, 68.95 kPa internal pressure and fully buried forms the reference leak amplitude to which the other cases are normalized. When the leak rate increases due to the increase in internal pressure or the hole diameter, the leak amplitude increases accordingly.

Understanding the changes in AE response with pipeline condition is critical to estimate the sensor spacing and the threshold for detectable leak size. Assuming that the attenuations due to spreading and absorption in the laboratory pipe are negligible for the selected source-sensor distance, Figure 7 and Table IV can be used as a guide to define the discrete sensor spacing if the attenuation coefficient of a pipe is known. The attenuation coefficient can be obtained numerically or experimentally using a simulated signal (e.g. ultrasonic wave generated with a transmitter) on the pipe. The leaks AE amplitudes are driven for a specific pipe geometry and leak simulator design. It is important to note that the amplitudes may show some variations depending on the pipe thickness and geometry of the leak hole (Laodeno et al., 2008).

The frequency contents of the leak waveforms are plotted in Figure 8 and Figure 9. The leak waveform due to orifice 1 has the peak frequency at 80 kHz while the leak waveforms due to orifices 2 and 3 have the peak frequency at 45 kHz. The difference may be because of the decrease in the leak rate or the change in the turbulence at the leakage point. It is important to note that the frequency domain plots are obtained using a 60 kHz resonant PZT sensor; therefore, the frequency spectrum is highly dependent on the sensor transfer function.

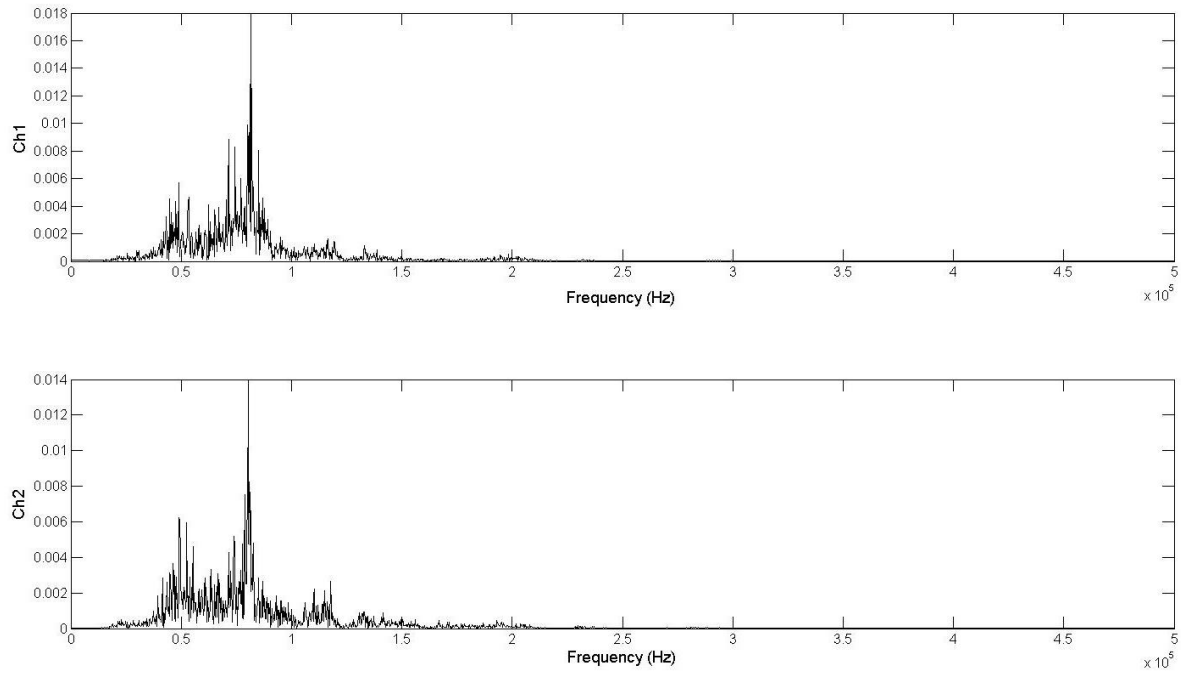


Figure 8. The frequency spectra of two AE sensors for the case of orifice 1, 68.95 kPa internal pressure and unburied pipe

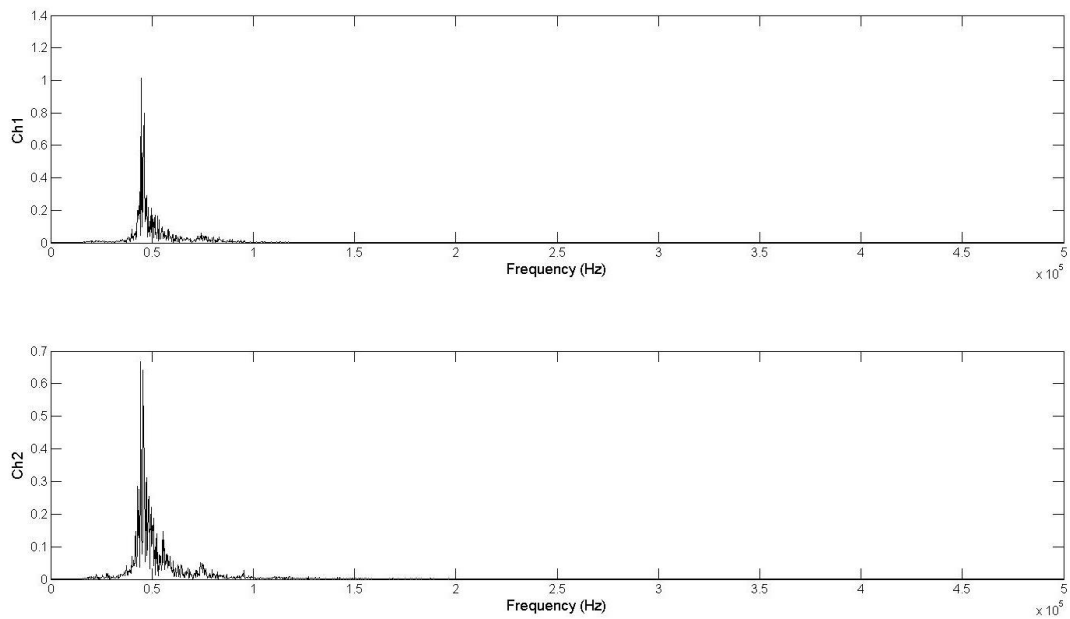


Figure 9. The frequency spectra of two AE sensors for the case of orifice 3, 68.95 kPa internal pressure and unburied pipe

3.2.4. Leak Location Accuracy

The arrival time difference is the most critical input to the leak location algorithm as there is no well defined arrival time of continuous emissions. The cross correlation function is typically used to determine the arrival time difference. However, this approach has limited success if the waveform includes reflected waves as in the case of this study as discussed in the introduction section. However, the AE method is a statistical method; therefore, an accumulation of an event cluster would be sufficient to pinpoint the leak location.

The cross correlation function for discrete and finite duration signals is defined as

$$R_{y_1 y_2}(\tau) = \sum_{t=1}^N y_1(t) y_2(t + \tau) \quad (3.1)$$

where $R_{y_1 y_2}(\tau)$ is the cross correlation coefficient of two signals, y_1 and y_2 , as a function of the time delay τ , N is the lengths of signals. The time delay becomes the input to the equation for linear localization as $x = \frac{\tau V(f, h) + L}{2}$, where L is the distance between the sensors and V is the wave velocity, which depends on the frequency and the pipe thickness. The equation is valid if the source to sensor path is straight. Ozevin and Harding (Ozevin and Harding, 2012) showed that the leak can be localized in multi-dimensional space using the linear localization equation and the geometric connectivity of the pipeline networks, which eliminates the need for a source-sensor direct path need. Using the equations above, the leak location in the model pipeline is identified. Table V, Table VI, Table VII show the average leak positions and standard deviations for all internal pressures, orifices and conditions. Figure 10 shows the event histogram for 68.95 kPa pressure, and 0.41 mm leak diameter in the unburied case. The actual leak position is at 45.7

cm. The most accurate result is obtained for partially buried pipe, orifice 1 at 344.75 kPa shown in Figure 11. The leak localization can be improved further using filtered waveforms and considering reflected waves through boundaries. Figure 12 shows the histogram for the fully buried with the 0.64 mm orifice and 68.95 kPa internal pressure.

TABLE V
Mean and Standard Deviations for Unburied Pipe in cm

Pressure(kPa)	Orifice Size		
	1	2	3
68.95	66.13±29.83	57.88±30.77	58.76±30.4
137.90	66.04±28.38	55.86±31.37	58.4±30.96
206.85	57.77±27.91	57.99±32.62	55.62±33.01
275.80	65.88±27.3	57.87±32.17	58.11±32.44
344.75	62.89±25.9	57.65±33.90	59.34±32.95

TABLE VI
Mean and Standard Deviations for Partially Buried Pipe in cm

Pressure(kPa)	Orifice Size		
	1	2	3
68.95	50.29±31.64	45.35±26.96	60.12±31.09
137.9	51.95±31.01	38.94±22.79	66.64±26.24
206.85	51.98±31.92	41.10±26.38	65.91±26.14
275.8	49.91±29.85	43.76±31.94	69.1123±28.3
344.75	45.31±11.37	57.98±30.66	67.59±28.29

TABLE VII
Mean and Standard Deviations for Fully Buried Pipe in cm

Pressure(kPa)	Orifice Size		
	1	2	3
68.95	51.93±28.49	61.17±34.48	45.65±32.08
137.90	42.95±29.86	61.66±34.12	50.23±37.48
206.85	46.83±31.36	63.01±33.29	54.21±37.57
275.80	48.39±30.53	62.76±34.42	59.46±36.47
344.75	48.98±29.48	56.14±36.08	66.27±25.48

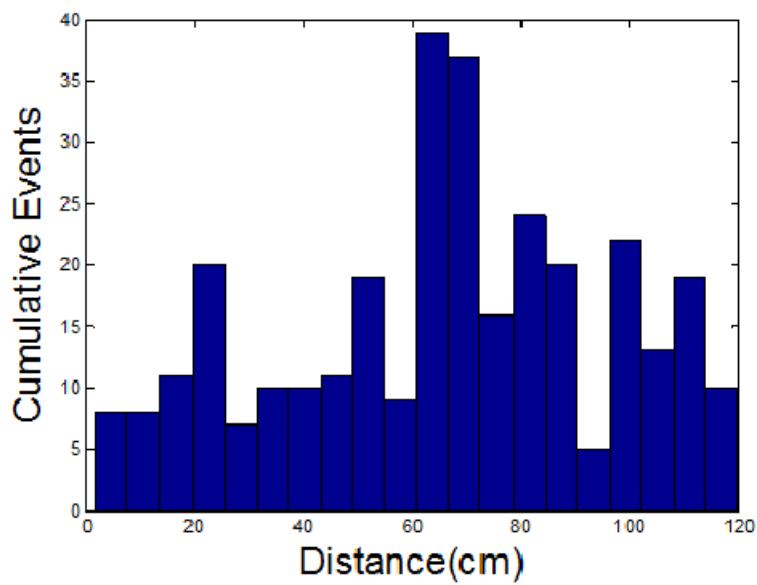


Figure 10. Leak location histogram example for unburied pipe

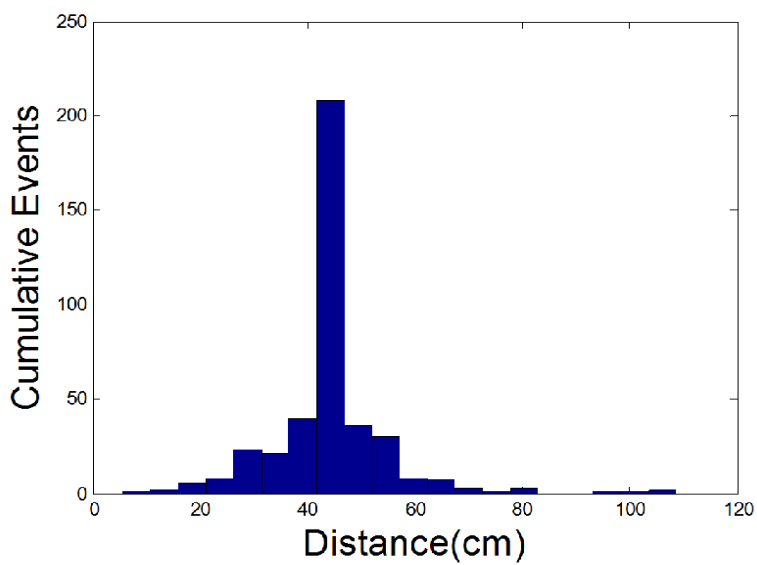


Figure 11. Leak location histogram example for partially buried pipe

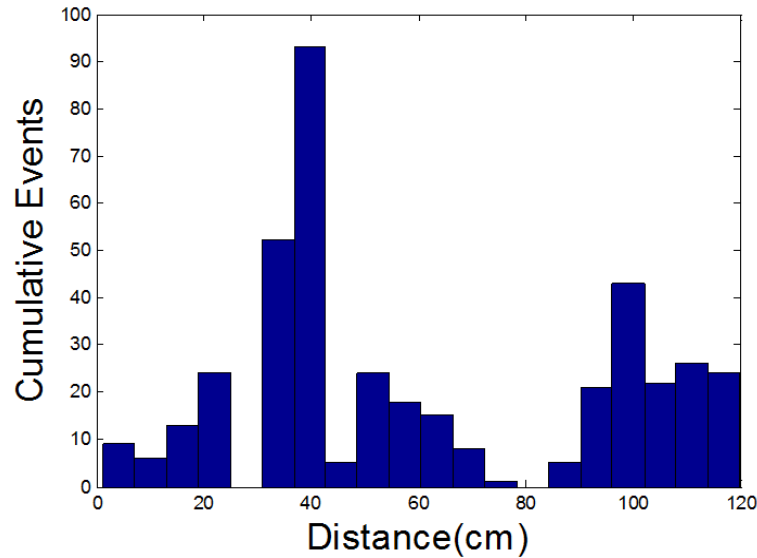


Figure 12. Leak location histogram example for fully buried pipe

The leak localization results are either around 45.7 cm or 60 cm. 60 cm is half of the length between the two sensors. Figure 13 shows the leak localization error versus wave velocity. The error is at minimum around 3000 m/s, which is the flexural wave velocity in steel. While cylindrical geometries have infinite wave modes, two wave modes dominate the response at low frequency: longitudinal and flexural wave modes. The wave velocity input is dependent on the sensing motion of the sensor used. In this study, the sensor used, R6, is sensitive to motion in normal mode. In this mode, flexural wave creates more displacement in normal direction compared to longitudinal wave. Additionally, the leak localization results are better when the pipe is either partially buried or wholly buried.

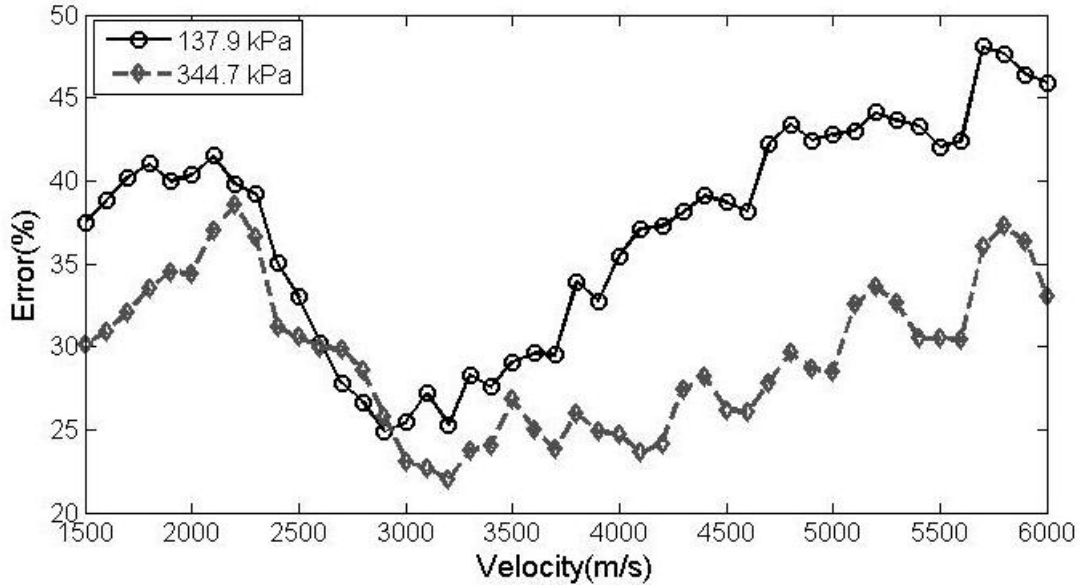


Figure 13. Leak localization error versus wave velocity

3.3. Numerical Model of the Pipeline Geometry

3.3.1. Characteristics of Numerical Model

Numerical models provide the flexibility to study wave propagation behaviors in various pipeline geometries. The solution of wave equations using numerical methods requires a delicate selection of mesh size and time step in order to prevent dispersion pollution, in other words incorrect mesh velocity. As a rule of thumb, $1/20^{\text{th}}$ of wavelength and inverse of maximum frequency are selected for mesh size Δx and time step Δt , which provides $V = \frac{\Delta x}{\Delta t}$, where V is wave velocity. Because of non-axisymmetric loading, the geometry is modeled in three dimensions using symmetry to decrease the number of degrees of freedom. Quadratic

polynomial and tetrahedral elements are selected for meshing. The numerical simulations are conducted using COMSOL Multiphysics Software.

Figure 14 shows the symmetric boundaries and the density of meshing. The pipe diameter and thickness are the same as the laboratory model. To understand the wave attenuation profile, a numerical pipeline mode of 3.35 m is created. The mesh size and time step of loading functions with two different frequencies are given in Table VIII. For 60 kHz loading, the mesh size and time step are set as 3.33 mm and 1.11 μsec , respectively. The loading function is defined by $F(t) = \sin(\omega t)e^{-(t-\tau)^2/\tau^2}$ where ω is circular frequency, and τ is the period of modulated signal taken as the period of the peak frequency.

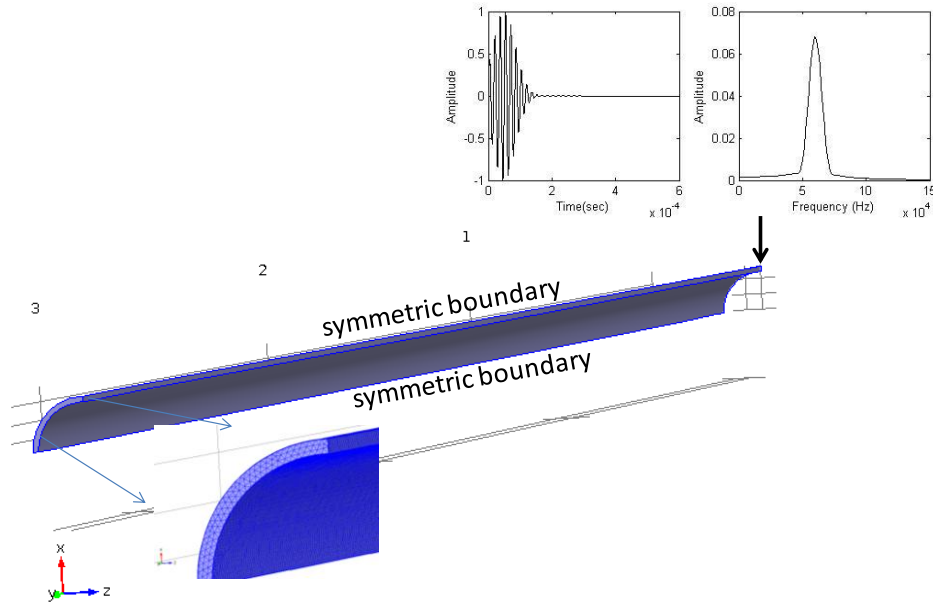


Figure 14. Finite element model showing the mesh density and the loading function for 60 kHz loading.

TABLE VIII
Mesh, Time Step and End Time of the Loading Function

Loading Frequency	Assumed Wave Velocity(m/s)	Mesh(mm)	Time Step (μ sec)	End Time (ms)
10 kHz	1500	7.5	5	4
60 kHz	3000	3.3	1.1	3

Loading with two different frequencies, 10 kHz and 60 kHz are applied at out-of-plane direction at the end of the pipe model. The attenuation curve is obtained with the change in the maximum amplitude of displacement in the respective direction. The wave propagation velocity is dependent on the frequency and the thickness of the medium. With the decreasing frequency, there is a decrease in the wave velocity. At 10 kHz, the wave velocity is assumed to be half of the wave velocity at 60 kHz. The coating material and other damping sources such as connections can be included into the model to obtain the attenuation curves. Table VIII summarizes the finite element model variables for two frequencies.

3.3.2. Waveform Signatures and Attenuation Curve

Figure 15 shows two displacement histories in the direction of loading at 0.8 m and 1.1 m away from the source of the 60 kHz loading. Based on the first arrival of waves at 0.8 m, the wave velocity is calculated to be approximately 2600 m/sec which agrees with the expected value. The load function applied at the end of pipe is in radial direction; however, due to asymmetric nature, it causes displacements in all directions. Therefore, a complex waveform

signature is obtained. At some locations, the wave is distorted because of overlapping of various wave mode arrivals.

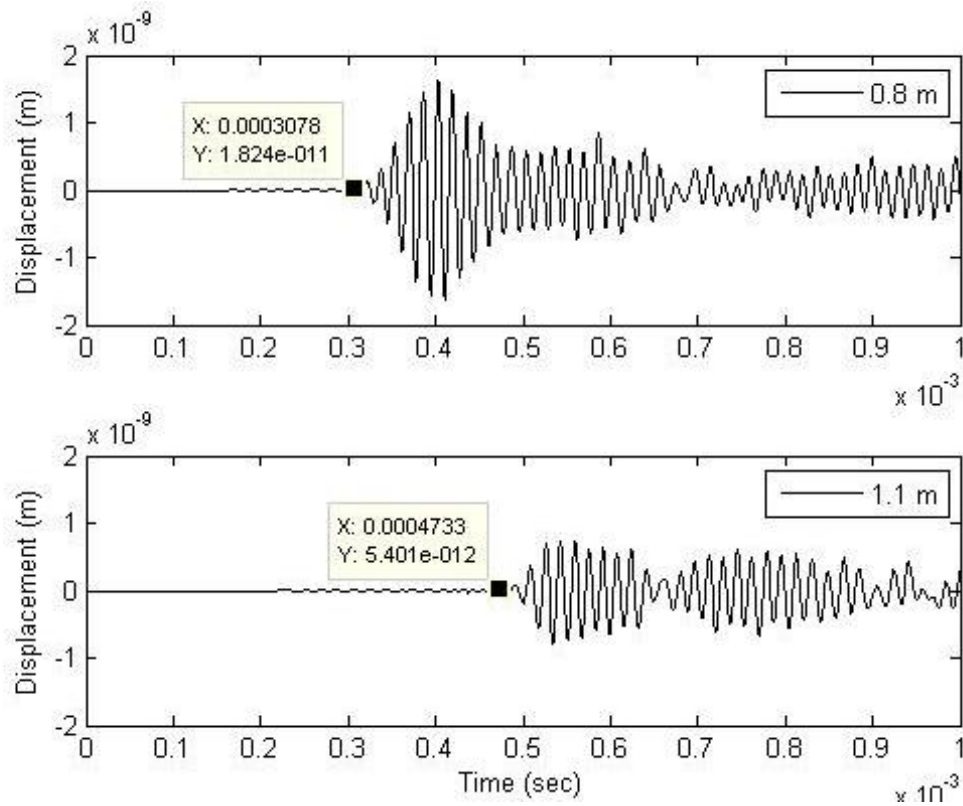


Figure 15. Displacement histories for out of plane 60 kHz loading 0.8 m and 1.1 m away from the source

Figure 16 and Figure 17 show the displacement histories at out-of-plane (r) and in-plane (z) directions for points 0.8 m and 1.1 m away from the source for 10 kHz excitation frequency. The wave velocity is calculated about 1650 m/s. The maximum displacements in the z direction are 20% of the r displacements in magnitude for the two points shown in the figures. The load is

applied in the r direction; therefore, it causes higher displacement at the r direction as compared to the z direction.

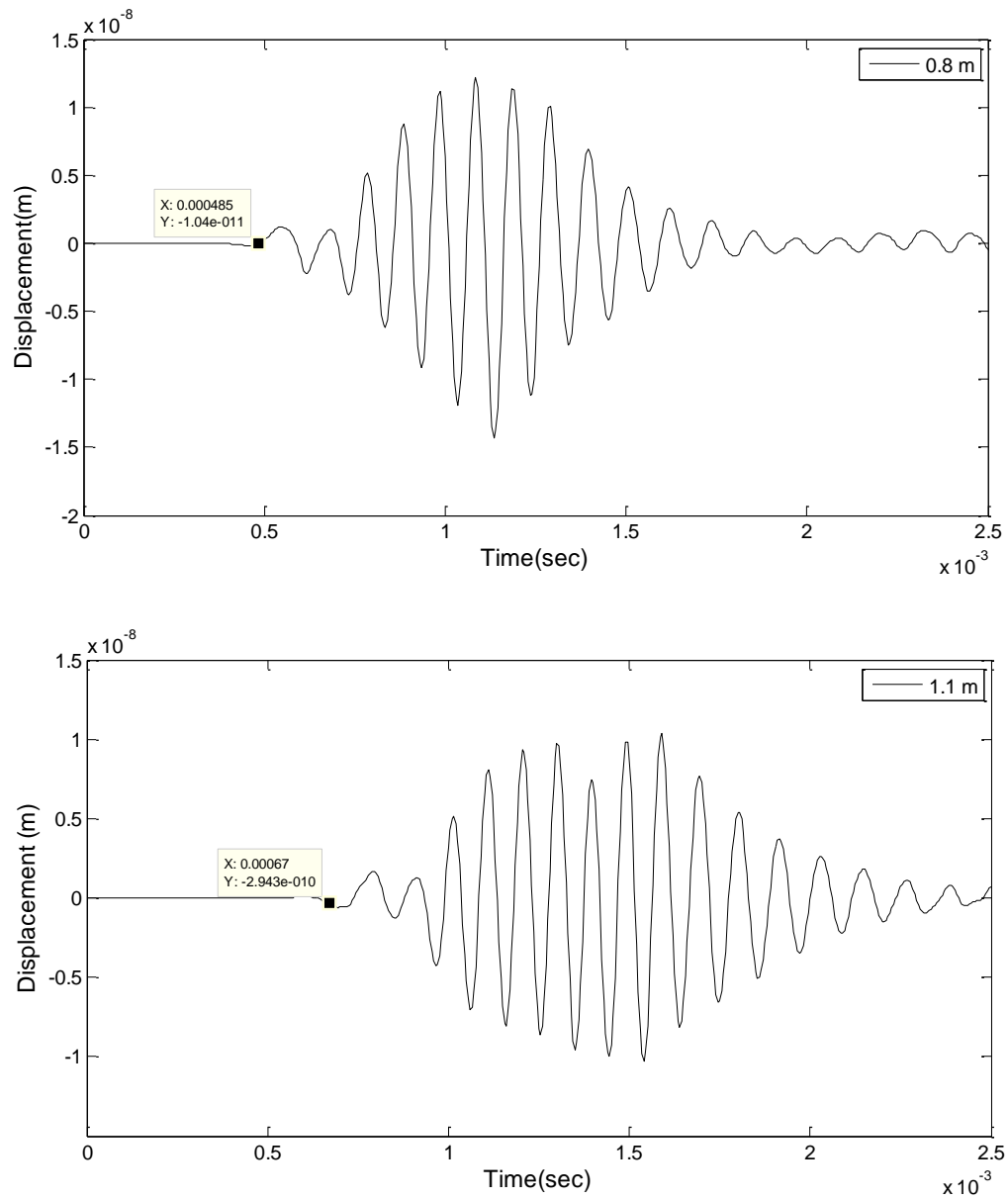


Figure 16. Displacement histories for out of plane 10 kHz loading 0.8 m and 1.1 m away from the source

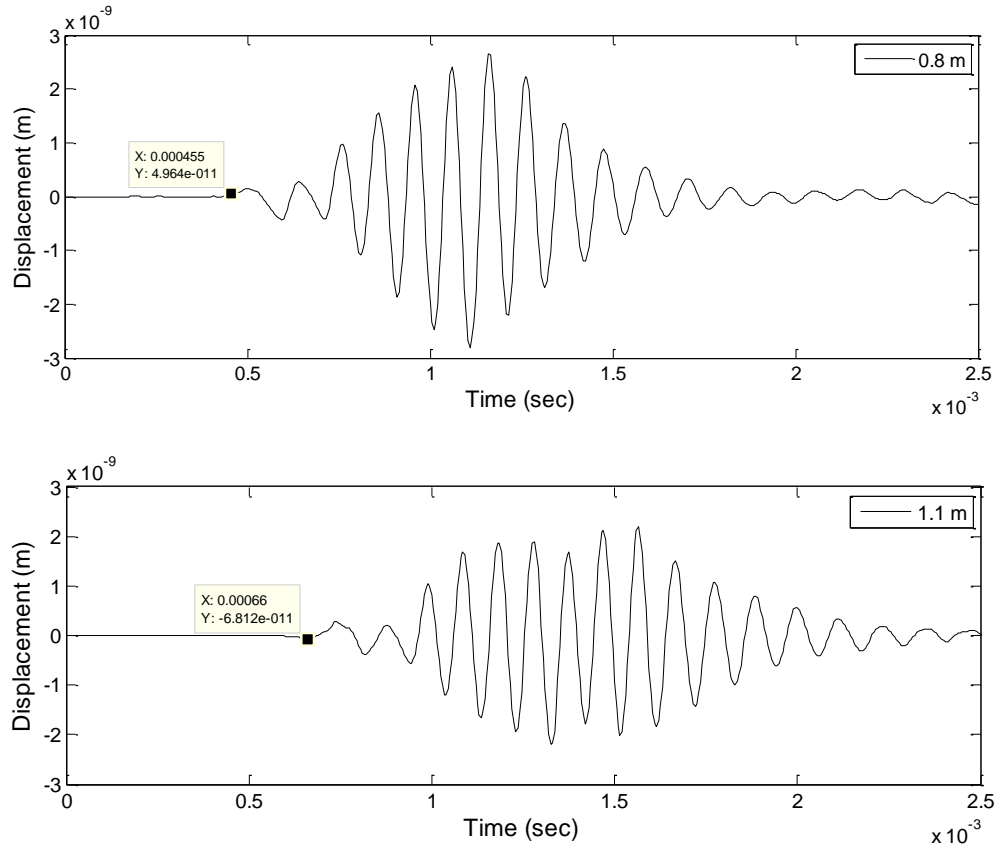


Figure 17. Displacement histories for in plane 10 kHz loading 0.8 m and 1.1 m away from the source

Figure 18 shows the maximum displacement values at every 0.1 m away from the source for 60 kHz and the exponential curve fit with the equation as $A(m)=1.29E-9\exp(-0.1929x)$. The attenuation coefficient $\beta(60kHz)$ as -0.1929 causes a dB loss of 1.68 dB/m using the equation $dB = 20\log(\beta(60kHz)x)$. As an example, for the unburied pipe and orifice 1 with 68.95 kPa internal pressure, the amplitude is 58 dB. Assuming the minimum threshold to be 35 dB, the required sensor spacing is about 14 m. The attenuation coefficients both in the r and z directions

using the load in the r direction are calculated similarly for 10 kHz frequency, and the results are summarized below.

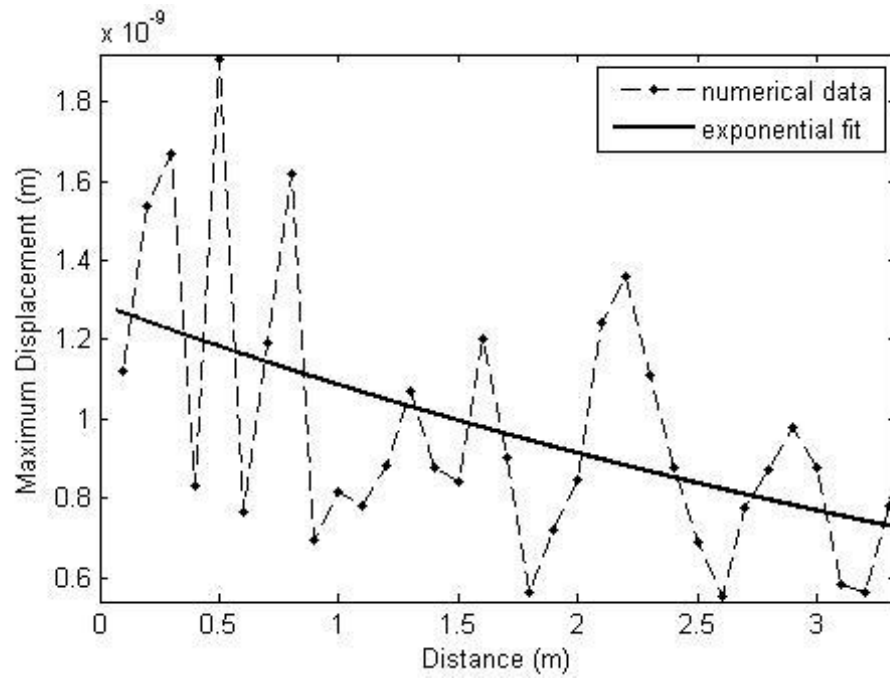


Figure 18. Attenuation curve in r direction and exponential curve fit for 60 kHz

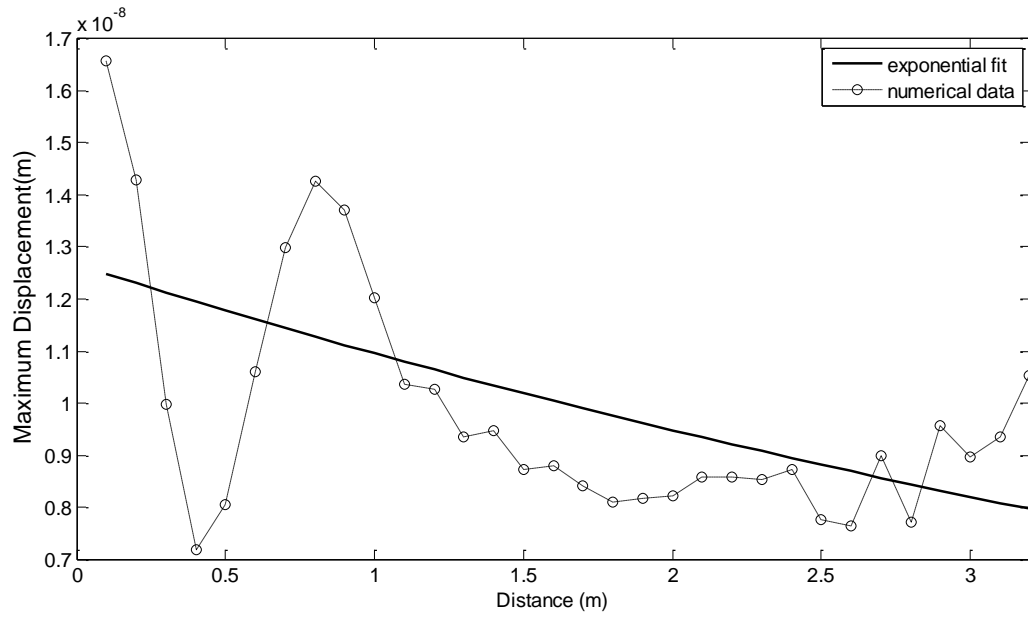


Figure 19. Attenuation curve for 10 kHz loading in r direction

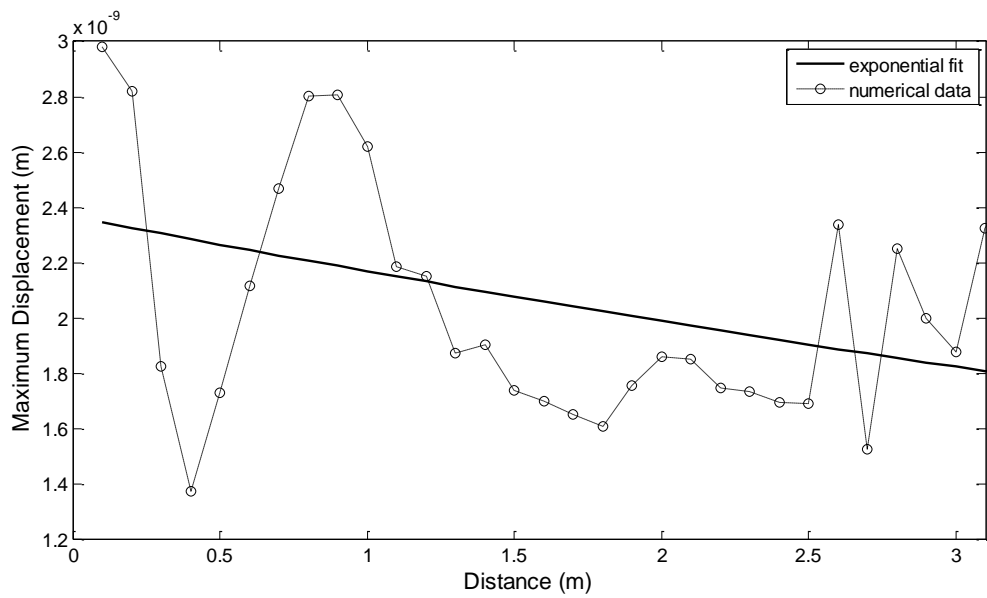


Figure 20. Attenuation curve for 10 kHz loading in z direction

Table IX summarizes the exponential curve fit equations and loss factors for three cases. For 10 kHz, the loss in dB/m in the z direction is 60% of the r direction, which increases the sensor spacing for the unburied pipe and orifice 1 with 68.95 kPa internal pressure. The sensor spacing is about 18 m and 31 m for 10 kHz loading in the r and z directions, respectively. The sensor spacing for 10 kHz is calculated with the assumption that the 10 kHz sensor response is similar to the 60 kHz sensor response utilized in the experimental section of this study.

TABLE IX
The Loss in dB/m for 10 kHz and 60 kHz Loading

	Out-of-Plane(r)		In-Plane(z)	
Loading Frequency	Exponential fit Equation	Loss(dB/m)	Exponential fit Equation	Loss(dB/m)
10 kHz	$1.267\text{E-}8e^{-0.145x}$	1.26	$2.367\text{E-}9e^{-0.08664x}$	0.75
60 kHz	$1.29\text{E-}9e^{-0.1929x}$	1.68	$5.39\text{E-}10e^{-.1062x}$	0.92

3.4. Discussion and Conclusion

The identification of sensor spacing for leak localization is studied using experimental and numerical data. The experiments on a small scale pipe provide the AE amplitudes at

different leak rates and pipeline conditions; the numerical method calculates the attenuation coefficients for the particular geometry and frequency. For different sensors, the AE leak amplitude at near field can be estimated through the comparison of the sensor sensitivities. For different frequencies, the numerical study can be repeated to obtain the attenuation coefficient and to identify the sensor spacing.

CHAPTER 4

DESIGN, MODELING AND CHARACTERIZATION OF PIEZOELECTRIC AE TRANSDUCER

4.1. Introduction

As discussed earlier, the sensor response characteristics play a significant role in detecting and locating the leak with long-range sensor spacing. This chapter discusses the design, modeling and characterization of a particular geometry piezoelectric AE sensor in order to increase the required sensor spacing for leak detection and localization as compared to conventional cylindrical piezoelectric AE sensors. A finite element model of the piezoelectric sensor is built to identify the resonant frequencies using the frequency domain analysis. The coupled response of the sensor on a pipe is obtained using multiphysics models (structural and piezoelectric) and compared with the response of the conventional AE sensors. The electromechanical characterization result using an impedance analyzer is compared with the numerical result. The sensor is tested on the pipe for leak detection and location. The directivity of the transducer is shown under the Q-switched ND-Yag laser source.

4.2. Finite Element Models of Piezoelectric Transducer

4.2.1. Transducer Design

The conventional acoustic emission transducers have cylindrical shape with varying height and diameter. The sensing direction is controlled by the poling direction of the piezoelectric ceramic. The most common AE sensors operate at thickness mode, which is sensitive to out-of-plane motion with respect to the propagating elastic waves. However, in cylindrical, plate-like geometries, this direction of sensing corresponds to the most dispersive longitudinal plate mode for frequencies less than 100 kHz, L(0,1) (Luo,2005). In order to increase the discrete sensor spacing to monitor long pipeline structures, the transducers should be sensitive to tangential or in-plane motion with less attenuative characteristics (shown in the previous chapter numerically), which corresponds to the longitudinal L(0,2) mode. In this study, the advantage of the high piezoelectric coefficient in the thickness mode of PZT is utilized as the transducer is sensitive to in-plane motion through a special geometry design.

The design criteria of the transducer are the resonant mode at thickness direction as 60 kHz (controlling thickness t , diameter D and cut length x) and placement on non-conforming surfaces (controlling cut length x) in the direction of poling as shown in Figure 21.

The element dimension coupled to the surface should also be smaller than the wavelength to prevent the aperture effect. Two parameters to consider in order to select the material for AE sensing are the piezoelectric coefficient g and the mechanical impedance match. The material is selected as PZT- 5A because it has one of the highest g_{33} coefficient among the soft piezoelectric materials. The mechanical impedance of steel is in the range of $23.55 - 39.15 \times 10^6 \text{ kgm}^{-2}\text{s}^{-1}$

which is close to the mechanical impedance values of the piezoelectric ceramics listed in Table X, provided by American Piezoelectric Ceramics (APC).

TABLE X
The Properties of Two common PZT Ceramics Used for Sensing

Piezoelectric Ceramic	Mechanical impedance ($10^6 \text{ kgm}^{-2}\text{s}^{-1}$)	Piezoelectric Charge Constant (10^{-12} CN^{-1})			Piezoelectric Voltage Constant ($10^{-3} \text{ m}^2/\text{C}$)		
		d_{33}	d_{31}	d_{15}	g_{33}	g_{31}	g_{15}
PZT-5A	35.65	400	-175	590	24.8	-12.4	36
PZT-5H	34.5	630	-276	720	21	-9	27

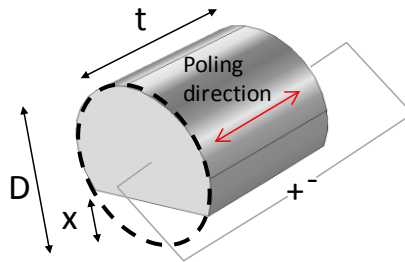


Figure 21. Geometric variables of piezoelectric transducer

The finite element model of the transducer geometry is studied using a frequency domain analysis to identify the dimensions. The electrical boundary conditions of the transducer are defined as an AC electric potential at one end of the transducer and the ground terminal at the other end. The AC voltage is applied as electrical load $V_{ac}(\omega)$ to the piezoelectric transducer:

$$V_{ac}(\omega) = V_{DC}e^{i\omega} \quad (4.1)$$

The constant voltage V_{DC} is taken as 1 V while the circular frequency ω is swept to have the frequency range of 1 kHz to 200 kHz with 1 kHz increments. When the electrical frequency matches with the resonant frequency of the transducer, the transducer's response is amplified. Using the material properties of PZT-5A and the varying three geometric variables, the transducer dimensions, thickness, diameter and cut length are identified as 20 mm, 20 mm and 5 mm, respectively. The local coordinate system is modified in order to orient the poling direction with g_{33} properties of PZT-5A as shown in Figure 22. The average electrical displacement at the terminal is plotted in Figure 22. The electrical field in $-y$ direction (sensing direction) is amplified near 60 kHz. As structural damping is not introduced in this early model, the resonance has a sharp behavior. Figure 22 also shows the mechanical displacement at 60 kHz. The red color shows the highest displacements on the sensor. The sensor displaces the most at the ground and terminal surfaces at 60 kHz.

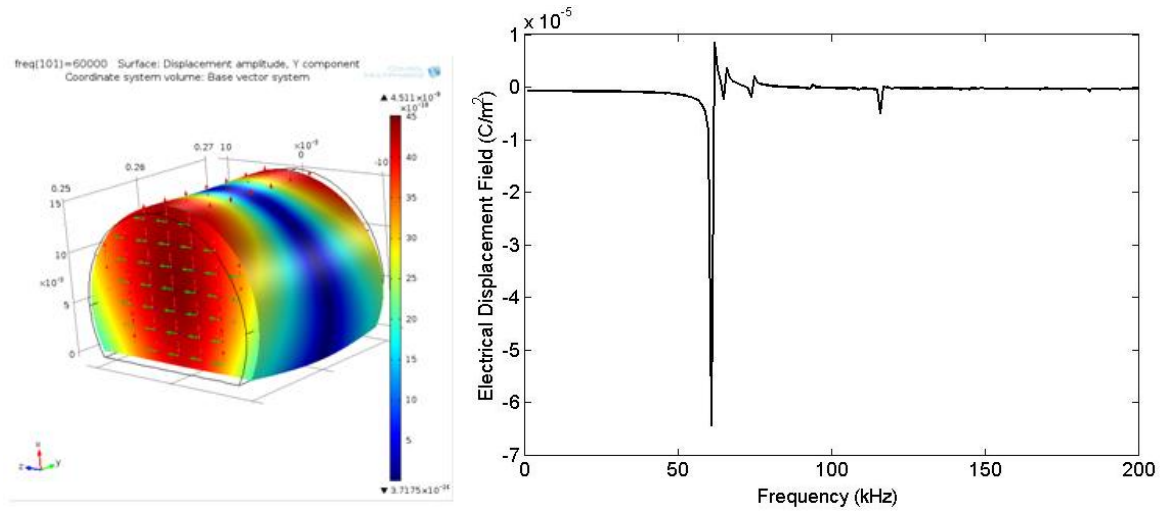


Figure 22. Frequency domain model and the response history

4.2.2. Multi-physics Model for Steel-Coupled Response

In this study, the new transducer is defined as ‘cut-PZT’, the conventional cylindrical piezoelectric transducer is defined as ‘normal-PZT’. To compare the cut-PZT with the normal-PZT, the eigenfrequency and frequency domain analysis of the normal-PZT is done to determine the dimensions, diameter and thickness. The diameter and thickness is found to be 16 mm and 20 mm, respectively. Figure 23 shows the mode shape of the normal-PZT in poling direction at around 60 kHz. The electric displacement field is plotted in Figure 24 showing a very sharp peak around 60 kHz and another peak around 130 kHz.

The responses of two transducer geometries are evaluated when they are coupled to a steel pipe. A sinusoidal loading function at 60 kHz is applied in z (F_z) and r (F_r) directions as shown in Figure 25. The load function has about a six-cycle sinusoidal signal with 60 kHz

frequency and decay time of 5.3×10^{-5} seconds. In order to prevent the numerical dispersion and to reach the accurate solution, the mesh size is selected as $1/20^{\text{th}}$ of the wavelength, and the time step is selected as $1/20^{\text{th}}$ of the inverse of the target frequency. In this study, the mesh size and the time step are identified using 45 kHz frequency and 2700 m/sec velocity resolution and solved in a Mac Pro Server with 3.2 GHz Quad-Core Intel Xeon processor and 1 TB memory. Two symmetric boundaries are defined in order to reduce the required number of degrees of freedom, shown in Figure 25. The other boundaries are defined as natural boundary conditions. The poling directions are defined as in r direction for normal-PZT and z direction for cut-PZT. Due to the circular geometry of the pipe, a thin adhesive layer is defined between the pipe and the transducers in order to realize actual coupling condition of a pipe testing. While no specifications for the adhesive used in the laboratory experiments are found, the elastic properties of a similar adhesive are found from the literature as 3.66 GPa for Young's Modulus, 1.22 g/cm^3 for density and 0.36 for Poisson's ratio (Cease et al., 2006).

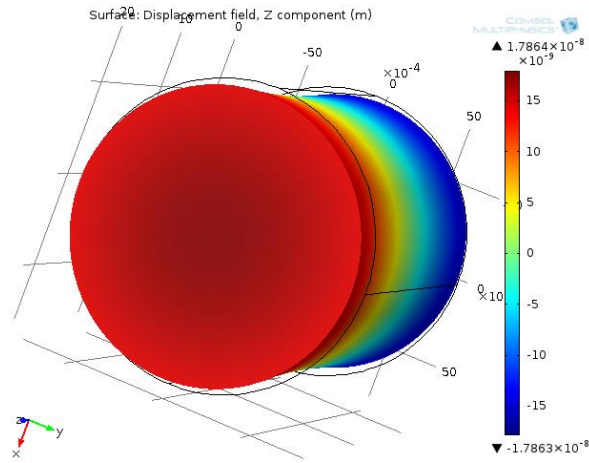


Figure 23. Displacement around 60 kHz

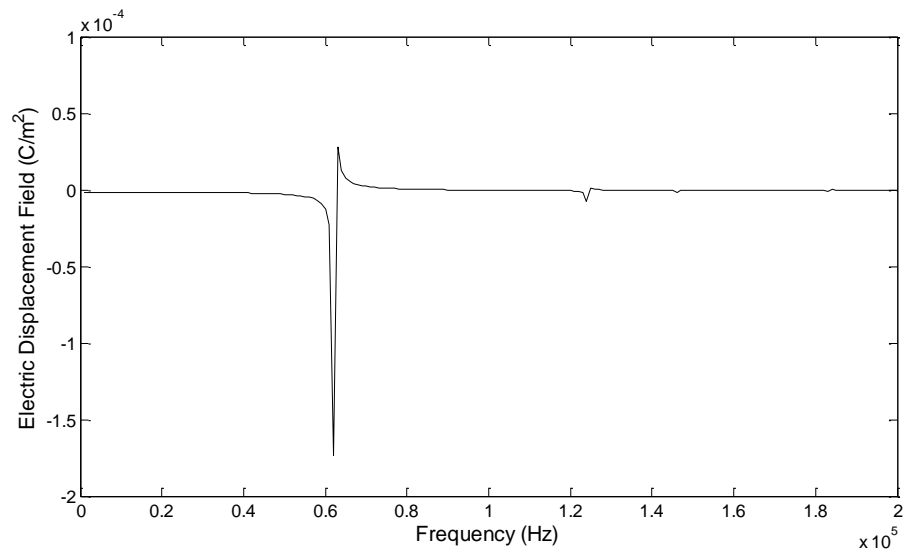


Figure 24. Electric displacement field of normal-PZT

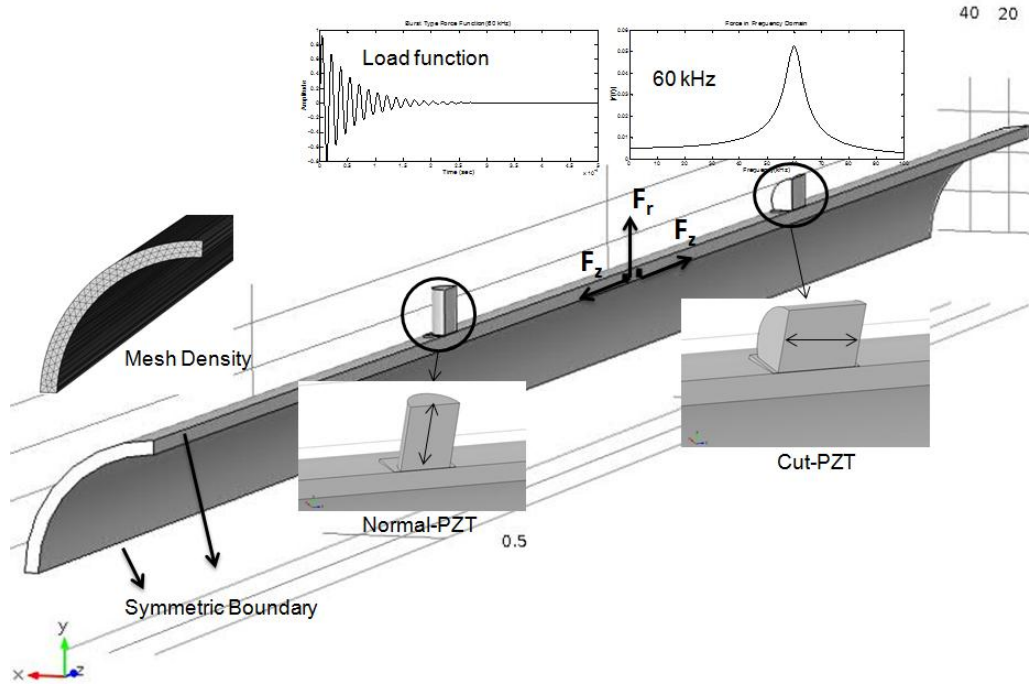


Figure 25. Finite element models on a pipe geometry coupled with cut-PZT and normal-PZT

The pipe material is defined as structural steel, and the PZT-5A properties listed in Table X are utilized. The ground and terminal of each transducer are defined as two ends of a cylindrical element in order to perform the coupled mechanical-electrical model and obtain the electric potential outputs. The constitutive equations of the piezoelectric material for sensing are shown in Chapter 2.

The stress tensor is obtained by the dynamic response of the piezoelectric transducer under surface acceleration. The surface acceleration is the outcome of the forced vibration model of the pipe using an elastic material model. The electric potential histories under F_z and F_r loadings indicate the directional sensitivities of the transducers.

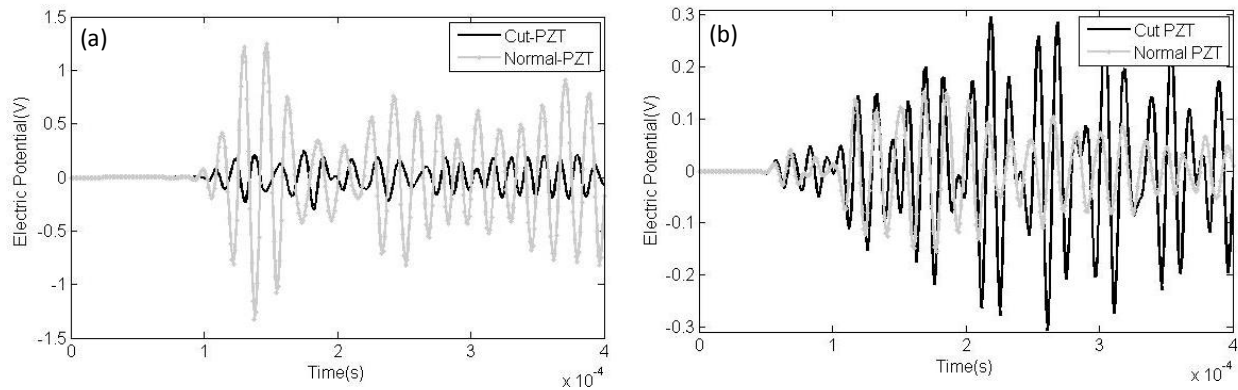


Figure 26. Electrical potential histories for the 60 kHz load function in, (a) r direction, (b) z direction

Figure 26 shows the comparison of electric potential histories of cut-PZT and normal-PZT under 60 kHz cyclic loading with 1 N amplitude at out-of-plane (r) and in-plane (z) directions relative to the pipe geometry, Figure 25. For the r direction, the load is applied to the middle of the pipe. For the z directions, loads in opposite directions with 1 cm apart at the middle of the pipe are applied. The dimensions of the steel pipe are 127 cm in length, 5.11 cm inner radius and 0.6 cm wall thickness. The cut-PZT and normal-PZT are both placed 25.4 cm away from the loading point. In numerical model, the normal-PZT shows a maximum of 1.32 V and 0.15 V in a 0.4 ms time frame for the loading in F_r and F_z directions, respectively. For the cut-PZT, there is a small electric potential difference when the loading direction is changed from the r to z direction. However, the electric potential value, 0.31 V, obtained for the z loading is twice of the normal-PZT electric potential.

Figure 27 shows the response of the sensors under 10 kHz cyclic loading in the r direction. The response of the cut-PZT is low compared to the normal-PZT. The amplitude of the normal-PZT is 0.43 V, which is 33% of the response under the 60 kHz loading. This result agrees with the experimental result. The sensor response decreases substantially when the source frequency is away from their resonant frequencies.

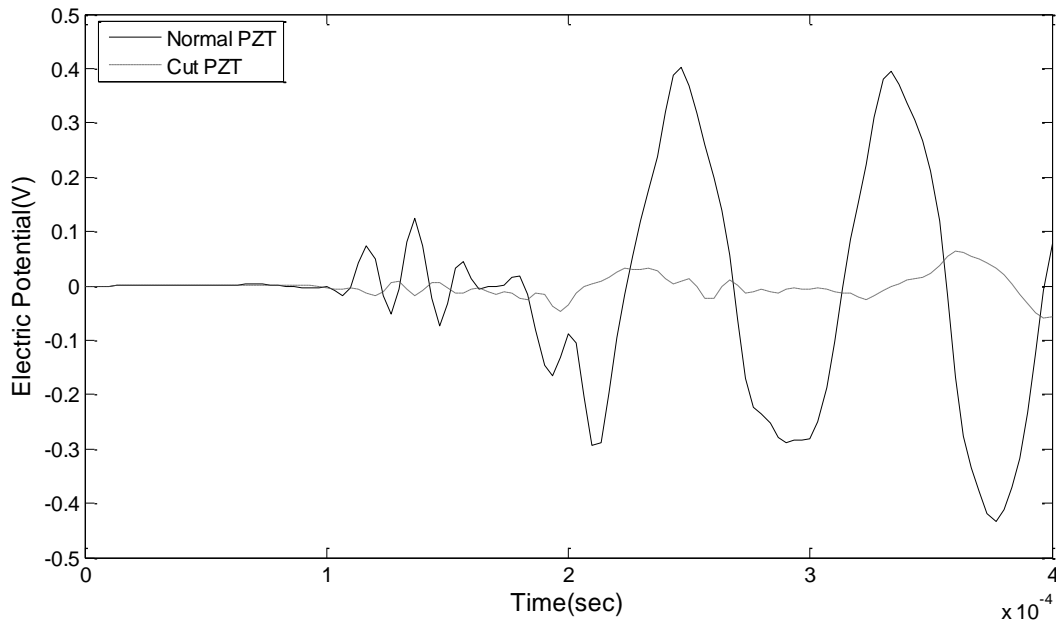


Figure 27. Electric potential under 10 kHz loading

4.3. Characterization Experiments

4.3.1. Impedance and Bandwidth Measurement

Three cut-PZT transducers are tested using the Agilent 4294A Precision impedance analyzer to identify the repeatability of the transducer design. The frequency sweep range is defined as 1 kHz to 150 kHz. When the mechanical resonance of the PZT ceramic matches with the input frequency, the response is amplified based on the quality factor of the transducer. Figure 28a shows the admittance plots of three transducers which show the repeatability of the transducer response. Peaks are observed at 60 kHz, 66 kHz, 76 kHz and 117 kHz. The sharpest peak is at 60 kHz. The average of three measurements is taken, and the numerical result is modified with a 3% isotropic damping for matching with the experimental result, shown in Figure 28b. The results indicate accuracy of the numerical model for the transducer design.

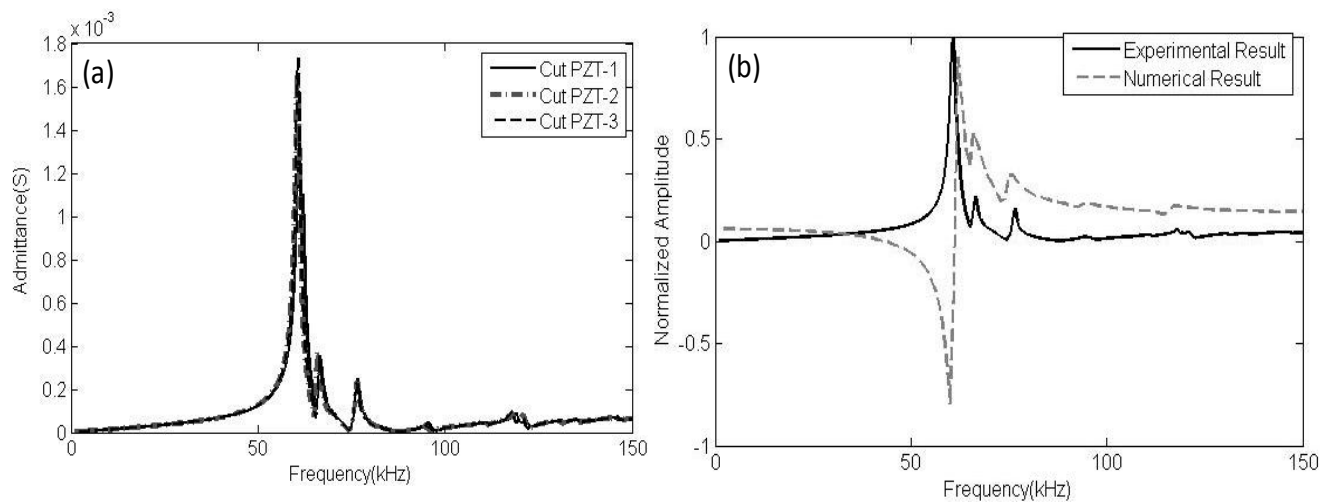


Figure 28. (a) Admittance results of three cut-PZT sensors, (b) the comparison of average result with the numerical model with 3% isotropic damping

The mechanical quality factor Q_m is measured by the ratio of the equivalent reactance to the equivalent resistance of losses in vibrating element using the following equation:

$$Q_m = \frac{f_n^2}{2\pi f_m Z_m C (f_n^2 - f_m^2)} \quad (4.2)$$

where f_n and f_m are frequencies at maximum and minimum impedances of element, respectively, (Hz), Z_m is minimum impedance of the element (Ω), and C is element capacitance (F) measured at 1000 Hz. Based on the experimental data, the mechanical quality factor of the transducer is identified to be 24.02 using Z_m as 976.9 Ω , f_n as 87.12 kHz, f_m as 60.00 kHz, C as 215 pF. The transducer bandwidth at -3 dB of the admittance peak ranges from 59.9 kHz to 61.4 kHz. Based on the formulation of the quality factor as $f_r/\Delta f$, the quality factor is calculated to be 40. The calculated isotropic damping as 3% (Q_m -33.3) to match the numerical result with the experimental result shows that the three measurements of quality factor are in agreement. The value is lower than the reported value (Q_m -80) of PZT-5A by the manufacturer.

The AE transducers are coupled to the tested medium using adhesive or temporary couplant in order to fill the voids and provide a good acoustic path. Therefore, it is important to understand the transducer behavior when the mechanical boundary condition is modified due to the coupled state to another structural medium. The transducers are tested in the free case and then coupled to a steel plate using vacuum grease, Figure 29. When the transducer is coupled to a steel plate, the second and the third harmonics at 66 kHz and 77 kHz disappear, and the response at the fundamental resonance mode becomes noisier. The similar behavior is observed for adhesively coupled transducer.

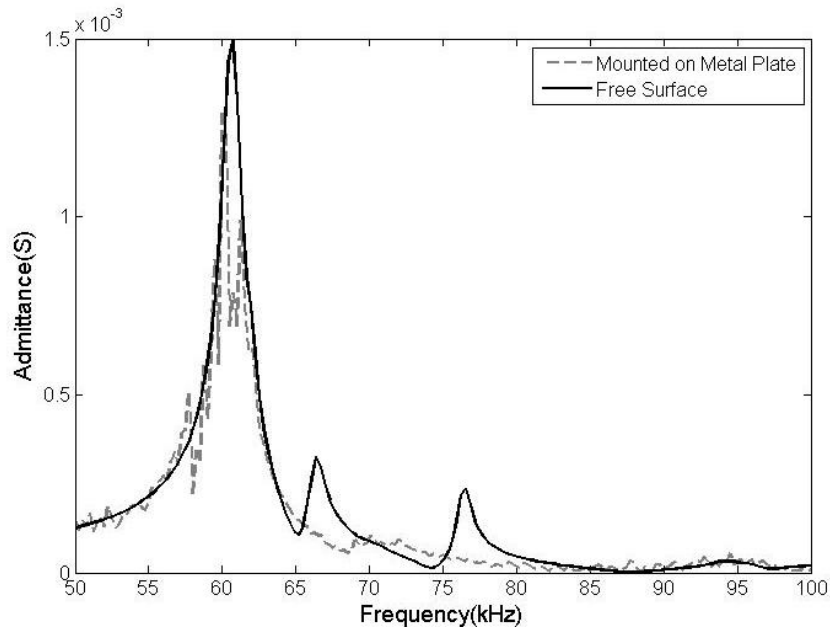


Figure 29. The comparison of the transducer response to free boundary and coupled boundary to a steel plate

4.3.2. Transducer Response to Varying Input Source

The cut-PZT and the normal-PZT transducers are coupled to the steel pipe using adhesive, and the responses under varying amplitude values of excitation source are recorded. The dimensions of the pipe are 11.4 cm diameter, 0.6 cm thickness and 152 cm in length. Figure 30 shows two loading directions $F_r(t)$ and $F_z(t)$. The ultrasonic excitation is created using another 60 kHz transducer and a function generator. The excitation signal properties are 60 kHz frequency, varying amplitude and 6 cycles with sine shape.

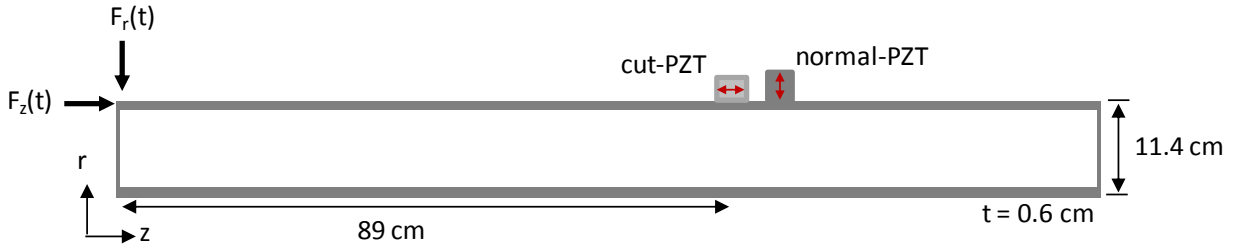


Figure 30. Experimental setup to study the transducer linearity

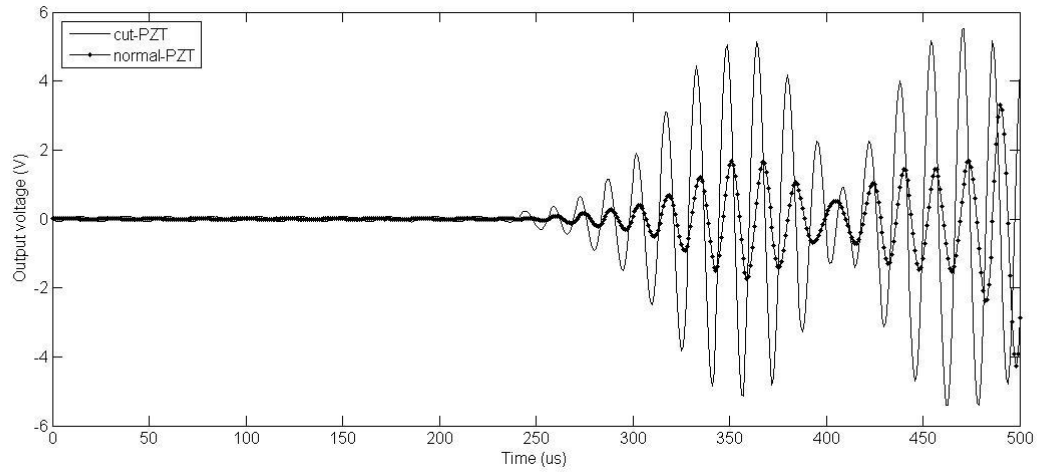


Figure 31. Waveforms (with 40 dB gain) recorded from cut-PZT and normal-PZT under 8 V excitation in z direction.

The outputs of two transducers are recorded using a PCI-8 board with the analog filter range from 20 kHz to 200 kHz. The data acquisition system is triggered by the function generator so that the arrival time indicates the length necessary for wave modes to arrive to the receiving transducers, cut-PZT and normal-PZT. Figure 31 compares the responses of two sensors under 8 V excitation in $-z$ direction. The first wave arrival is at 240 μs . The excitation envelope is clearly seen in the transducer outputs. The cut-PZT has higher response than the normal-PZT at the first arriving waves when the loading is z direction, which agrees with the numerical results.

The maximum amplitudes in the first 400 μsec time window of time traces are identified for loading in r and z directions and plotted under varying excitation amplitudes in Figure 32. Both sensors have linear responses and no hysteresis. For the loading in r direction, the amplitudes of the first arriving wave for both sensors are similar. However, for the loading in z direction, the amplitudes of the cut-PZT are higher than those of the normal-PZT because the cut-PZT is more sensitive to the motion in z direction.

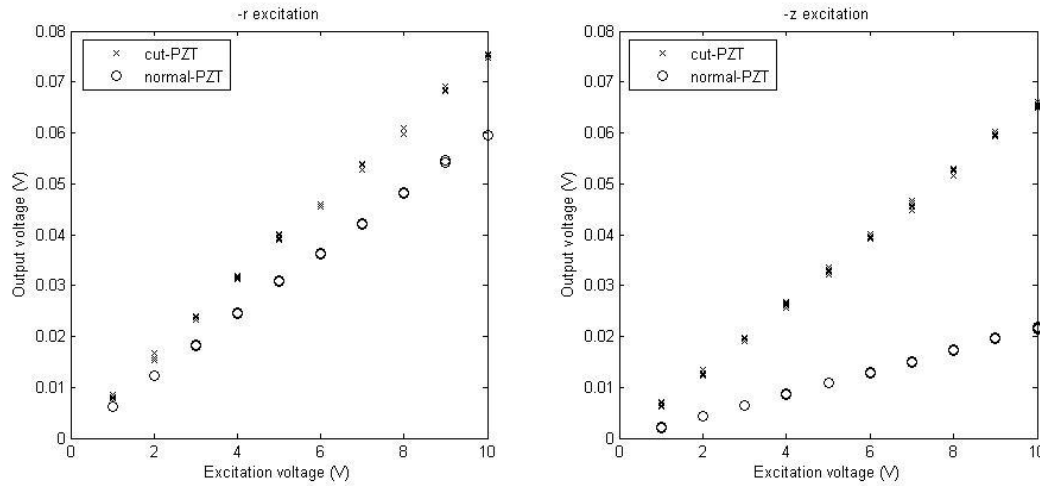


Figure 32. Output response of cut-PZT and normal-PZT for the 400 μ sec window under varying input loading

The same test is also conducted with the varying frequency from 10 kHz to 150 kHz with 10 kHz frequency steps. The loading source is a 6 cycle sine wave with the amplitude of 8 V. The actuator sensor is placed as shown in Figure 30 for the r and z direction loading. Figure 33 shows that for the given resonance range, the cut-PZT also gives higher amplitudes in the r direction. Figure 34 shows that in the z direction, cut-PZT gives higher amplitude if the loading frequency is more than 50 kHz. The frequency sweep test shows that cut-PZT has the highest amplitudes at 70 kHz while normal-PZT has the highest amplitude at 50 kHz in the r direction and 60 kHz in the z direction.

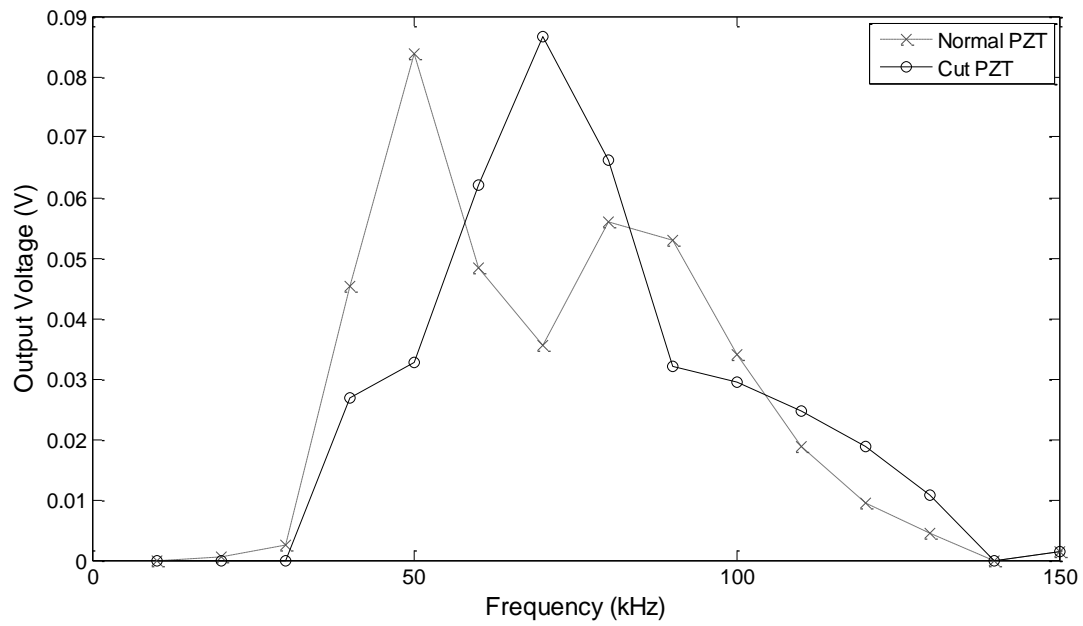


Figure 33. Frequency sweep for the loading in r direction on pipe

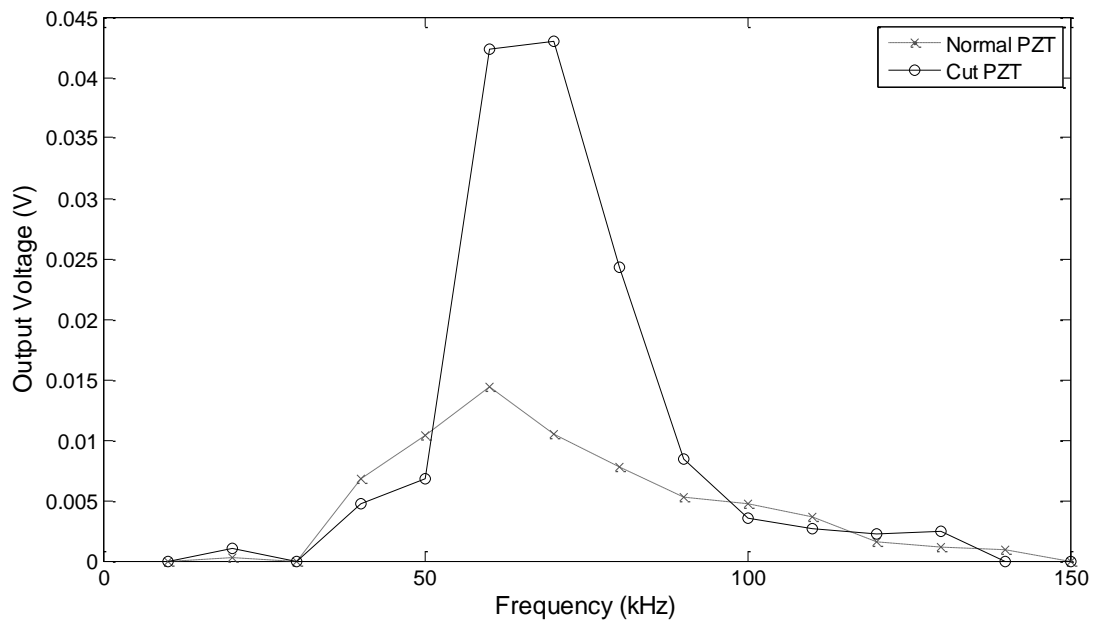


Figure 34. Frequency sweep for the loading in z direction

4.3.3. Directional Dependence with IR Laser-triggered Source

The ultrasonic waves are created on a half-cylindrical aluminum structure using Nd:Yag Q switched laser as shown in Figure 35. The laser is Polaris II, class 3b. The laser is mounted on an optical breadboard in order to control the beam direction and location. The laser energy, rise time and diameter are 50 mJ, 4-5 nsec and 3 mm, respectively. Because of the laser energy, laser beam diameter and the reflective index of the aluminum (>90%), the laser is in a non-ablation zone; therefore, the short pulse laser source creates wideband thermoelastic stresses with the Heaviside displacement function at the point of loading (Davies et al. 1993). Figure 35 shows a photograph of the experimental setup and schematic of the laser source point and the device under testing. Both the cut-PZT and normal-PZT transducers are tested with the same height as the laser beam to initiate the ultrasonic signal at the same level as the transducer. The transient data is recorded with high speed Tektronix MSO 2014, 4 channels, 100 MHz oscilloscope. The transducers are adhesively attached to the half aluminum cylinder with a 7.62 cm diameter and 15.24 cm height. The cut-PZT is directly attached while the normal-PZT has protective casing against electrical noise; therefore, its electric noise level is smaller than the cut-PZT.

In order to identify the directional response of the transducers, the angle between the excitation point and the transducer is varied through rotating the half-cylindrical structure. 0° is defined as the transducer at the epicenter of the block with respect to the source. The angle is varied with 10° increments from 0° to 90° .

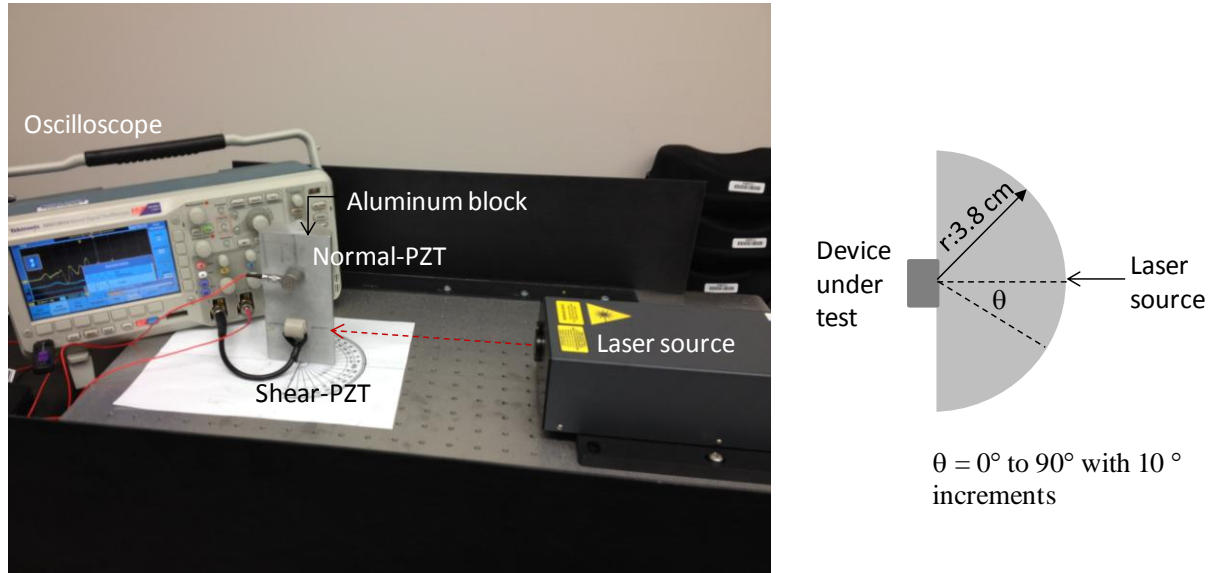


Figure 35. The identification of transducer directivity with laser-based system

Figure 36 shows the waveforms of cut-PZT and normal-PZT for three angles, 0° , 50° and 90° . The wave velocities of the pressure and shear waves in aluminum are 6150 m/s and 3100 m/s, respectively (Graff, 1975). The arrival time difference of two wave motions is about 6 μsec . Figure 36 highlights the arrivals of the P wave and the S wave for two transducers. The laser-induced thermoelastic stresses have high shear components. For the energy level studied and the excitation direction, the P wave has a smaller amplitude than the S wave. Figure 36a indicates that the cut-PZT has negligible response to the pressure wave while the transducer is mostly sensitive to the shear wave as expected. The waveform shape changes significantly with the direction of the source. There is about 90 degree phase difference for the shear wave between the 0° and 90° excitations. The waveform history at 90° is more complex than the waveform history at 0° . This might be because of the surface wave influence to the response of the former case. Figure 36b shows the responses of the normal-PZT to three angles. The phase change with the

angle is also observed in response of this transducer. However, this transducer has also significant responses to the shear wave in addition to the pressure wave which indicates the coupled sensitivity of the transducer to both thickness direction motion and tangential motion.

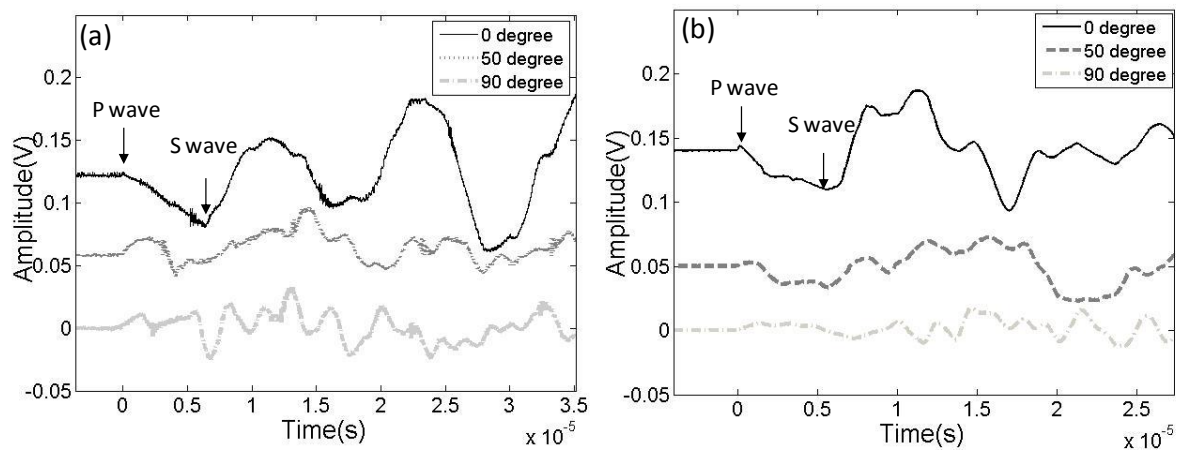


Figure 36. The waveform histories for 0°, 50° and 90° excitations; (a) cut-PZT,
(b) normal-PZT

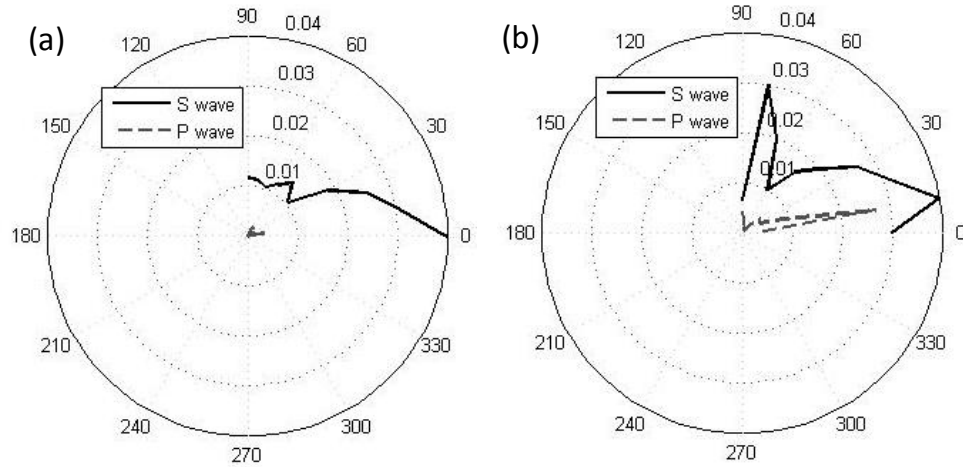


Figure 37. The amplitude responses in radial direction; (a) cut-PZT, (b) normal-PZT

The amplitudes of two wave motions for the excitation angles 0° to 90° with 10° increments are identified and plotted in a polar graph in Figure 37. The figure shows the directional dependence of the two transducers to the pressure and shear waves. The cut-PZT transducer has negligible response to the pressure waves while the highest response to the shear waves is at 0 degree. This agrees with the theory that the thermoelastic stresses due to the laser source cause mainly dipole shear stress (Bernstein and Spicer, 1999). On the other hand, normal-PZT has response to both pressure and shear waves with varying amplitudes. The highest response for both wave motions is observed to be at 10 degrees.

The identification of transducer directivity using a laser-based approach can be implemented in order to identify the waveform change with an angle so that the AE source orientation can be deduced by comparing the relative magnitudes of two wave motions and phase changes. The frequency spectra also vary depending on the source orientation with respect to the

transducer. For instance, Figure 38 shows the frequency spectra of three angles presented in Figure 36 in the time domain. The peak frequencies for cut-PZT and normal-PZT at 0 degree are 76 kHz and 25 kHz, respectively. The frequency response becomes wider when the angle is increased to 90 degree. The measurement clearly indicates that the frequency response is a function of the source angle when the transducers have narrow bandwidths.

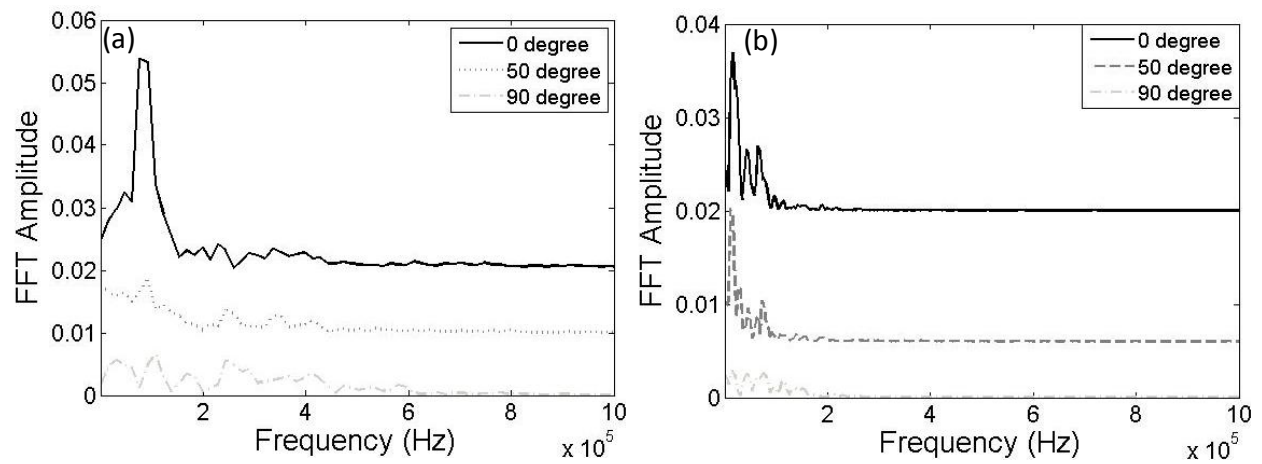


Figure 38. The frequency spectra for 0°, 50° and 90° excitations; (a) cut-PZT, (b) normal-PZT

4.4. Application on Leak Detection and Localization

Chapter 3 describe the experimental setup for leak detection and localization with varying pipe conditions using the normal-PZT (R6) transducers. In this section, the transducer responses of cut-PZT and normal-PZT to detect and locate leaks for the unburied pipe condition are

compared. The transducer responses are evaluated using a 1.27 mm orifice diameter to simulate the leak. Five different internal pressure values (68.9 kPa to 344.7 kPa with 68.9 kPa increments) are studied. The transducers are attached using adhesive and connected to 40 dB pre-amplifiers for the data acquisition system. The data is collected using a PCI-8 board.

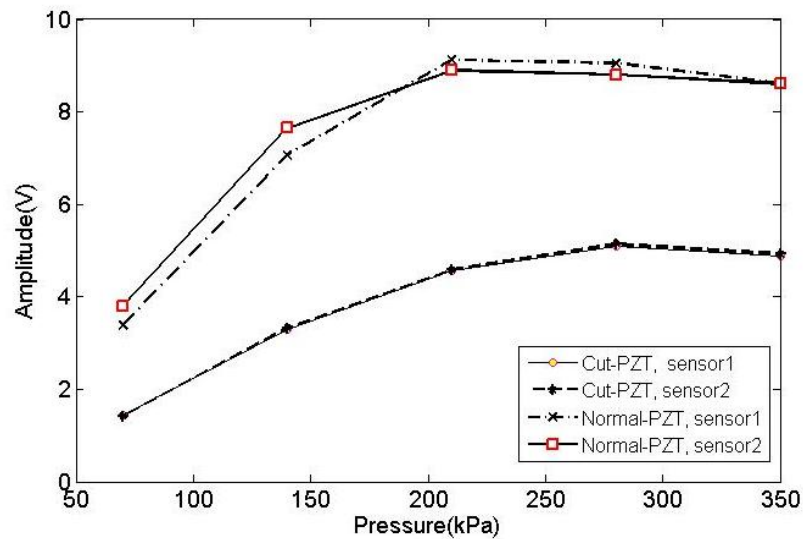


Figure 39. Leak amplitudes of cut-PZT and normal-PZT transducers for different internal pressures

Figure 39 compares the maximum amplitudes of two transducer types placed in pairs on the pipe with a certain distance. The cut-PZT transducer has a smaller amplitude than the normal-PZT transducer. This occurs because leak emissions have higher energy components for out-of-plane direction. Figure 32 shows that the transducers have linear responses to linearly

varying input functions while the leak amplitudes due to the varying internal pressure are not linear. This means that the increase in the internal pressure does not cause a linear increase in the AE amplitude. Two identical transducers are placed with distance to the leak at 76.2 cm (sensor 1) and 45.7 cm (sensor 2). No significant attenuation is expected at this sensor-leak distance difference. However, there are some variations in the maximum amplitudes of the normal-PZT transducers while the difference is negligible for the cut-PZT transducers. This is explained as the variations in the sensitivities of the cut-PZT transducers are smaller than those of the normal-PZT transducers.

As pointed out in Chapter 3, the leak localization requires the inputs of arrival time difference, wave velocity and sensor positions. The arrival time difference is measured using the cross correlation product of two neighbor transducers. To detect the delay between two transducers due to varying distances to the leak location, the channel waveform lengths are set to the same 4096 points with 1 MHz sampling frequency. Therefore, AE waveforms are independent from timing parameters needed for a conventional AE approach. It is recognized that this is an important measurement requirement for the cross correlation function to result in correct arrival time difference by bringing the identical waveforms of the two transducers together. The wave velocity varies depending on the sensitive direction of the transducer to the wave motion. The source localization is calculated with a sweep of velocities to find the correct wave velocity with the minimum error. Figure 40 indicates that 5000 m/s causes the smallest error for the cut-PZT transducer, while 2900 m/s is the ideal wave velocity for the normal-PZT transducer. The result agrees with the sensitivity directions of the two transducers to the wave motion.

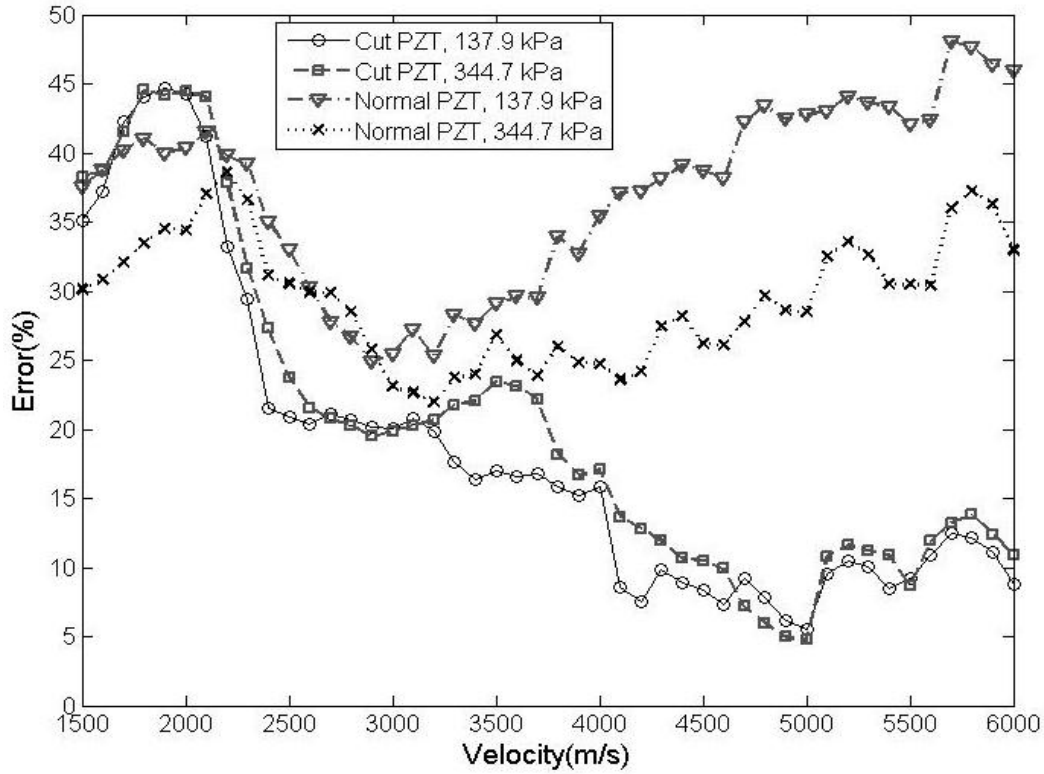


Figure 40. The source localization error with the sweep of wave velocity for cut-PZT and normal-PZT under 137.9 kPa and 344.7 kPa internal pressure

Table XI summarizes the average source location results with the percentage error of two transducers. The actual leak location is at 45.7 cm. The cut-PZT transducer has a smaller error than the normal-PZT transducer. This is because of the transducers' sensitivity to the less dispersive wave motion in the pipe.

TABLE XI

The Comparison of Leak Localization Ability of Cut-PZT and Normal-PZT for 1.27 mm Orifice Diameter

Pressure (kPa)	Cut-PZT		Normal-PZT	
	Location (cm)	Error (%)	Location (cm)	Error (%)
68.9	54.6	19.5	57.9	26.7
137.9	48.2	5.5	57.1	24.9
206.8	50.4	10.3	54.7	19.7
275.8	51.4	12.5	57.9	26.7
344.7	47.9	4.8	57.5	25.8

4.5. Conclusion

In this chapter, a particular geometry AE transducer is introduced in order to detect and locate leaks in pipelines with increasing the sensor spacing and decreasing the location error. The transducer has specific cut geometry to place on non-conformal structures to monitor tangential wave motion, taking advantage of the highest piezoelectric coefficient in the thickness direction. The transducer frequency response is numerically modeled and the comparison with the experimental admittance measurement shows perfect match through fitting the transducer frequency response with an isotropic damping coefficient. The mechanical response of the transducer is evaluated using a piezoelectric transmitter and found the linear output of the

transducer without any hysteresis. The directional dependence of the transducer to propagating wave motion is identified using laser-based simulations. The laser test results indicate that the cut-PZT transducer is mostly sensitive to shear waves while the conventional normal-PZT transducer has coupled responses to pressure and shear waves. The leak source localization is also improved using the cut-PZT transducer as the transducer is sensitive to the non-dispersive wave motion.

CHAPTER 5

CONCLUSION

5.1. Summary

The reliable method for leak detection in buried pipelines is an important problem to be solved for preventing catastrophic failures. Acoustic Emission (AE) is a highly sensitive, nondestructive testing method that relies on the propagating elastic waves created by leak turbulences. The method has a limitation of densely populated sensor distances for pinpointing the leak reliably. The objective of this thesis is to understand the leak characteristics and find an approach in order to increase the spatial positions of the sensors needed for pipeline networks.

The methods implemented include experimental and numerical components. For the experimental component, a laboratory scale pipe was built and the leak was simulated through a thickness induced orifice with varying diameters. The leak rate was varied by internal pressure and leak hole diameter. The effects of buried and on-ground pipes on the wave motion were studied. Amplitude curves were plotted for the increasing leak size, increasing internal pressure and increasing earth pressure. The errors of leak localization were presented in tables. A new piezoelectric sensor was developed with the objective of being more sensitive to less dispersive longitudinal wave motions. The sensor was characterized using electromechanical and mechanical tests. The performance was evaluated on the built pipe structure for leak localization accuracy. For the numerical component, an attenuation factor was found numerically for pipeline geometry with the same wall thickness and diameter as the laboratory scale pipe. The required sensor spacing was determined.

5.2. Findings

The major findings of this thesis are as follows

- The intensity of the AE signal generated by the leak decreases with increasing the earth pressure. Therefore, the sensor spacing for the buried pipelines should be less than the above-ground pipelines in order to detect the target leak size.
- The conventional piezoelectric sensors are sensitive to the displacement in normal direction with respect to the pipe surface. The attenuation coefficient is higher as compared to the wave motion in the tangential direction.
- A particular geometry piezoelectric sensor is designed to be sensitive to the wave motion in the tangential direction. The numerical model of the sensor agrees with the experimental results. The sensor has the first fundamental frequency in the thickness mode at 60 kHz. Due to the smaller attenuation characteristics, the new sensor allows for the increasing of the sensor spacing for both buried and above-ground pipelines.
- The leak localization results show that the new sensor provides more accurate leak localization as compared to the conventional piezoelectric sensors because of the sensitivity to the non-dispersive wave motion.

5.3. Future Work

The future work of this research is as follows

- The derivation of the attenuation profiles for three dimensional pipe geometry is computationally expensive. While the geometry is axisymmetric, the loading is non-axisymmetric. The numerical model for axisymmetric geometry with non-axisymmetric loading using the superposition of Fourier series will be developed with the spectral elements, which will allow for the obtaining of the attenuation coefficients for a range of pipeline geometries (diameter, thickness) and frequencies.
- The leak localization will be improved with a selective narrowband filter range and consideration of the pipeline boundaries in order to distinguish the first wave arrival and reflections for increasing the location accuracy.
- The piezoelectric sensor developed is tested on a 1.52 m pipeline and the leak localization is determined in 1D. The sensor will be tested on a longer pipeline in a field test with more than two sensors. The location algorithm will be revised for a longer pipe with more than two sensors for multi-dimensional localization.
- The sensor has currently high noise due to exposure of cables to the environment. The sensor will be packaged properly to increase the dynamic range for detecting smaller size leak rates.
- The sensor is sensitive to motion in tangential direction and the absolute calibration of shear mode sensors is not addressed in ASTM E 1316 (ASTM, 2011). Therefore, a new absolute calibration method will be proposed for determining sensitivity in normal and tangential directions through combining numerical and experimental results and the Q-switched laser source.

CITED LITERATURE

Ahadi, M. and Bakhtiar, M.S. (2010) "Leak Detection in Water-Filled Plastic Pipes through the Application of Tuned Wavelet Transforms to Acoustic Emission Signals," *Applied Acoustics*, Vol. 71, pp. 634-639.

Ahammed, M. and Melchers, R.E. (1995). "Probabilistic Analysis of Pipelines Subjected to Pitting Corrosion Leaks." *Engineering Structures*, Vol.17, No.2, pp.74–80.

American National Standard, ASTM E 1106-07 Standard Method for Primary Calibration of Acoustic Emission Sensors.

American National Standard, ASTM E 1316-11b Standard Terminology for Nondestructive Examination.

American National Standard, IEEE 176-1987, Standard on Piezoelectricity.

Beck, S.B.M., Curren, M.D., Sims, N.D. and Stanway, R. (2005) "Pipeline Network Features and Leak Detection by Cross-Correlation Analysis of Reflected Waves," *Journal of Hydraulic Engineering*, Vol. 131, No. 8, pp. 715-723.

Bernstein, J.R. and Spicer, J.B. (1999). "Line Source Representation for Laser-generated Ultrasound in Aluminum," *Journal of Acoustical Society of America*, Vol. 107, Issue 3, pp. 1352-1357.

Billman, L., Isermann, R., (1987) "Leak Detection Methods for Pipelines." *Automatica*, Vol.23, No.3, pp. 381-385.

Caleyo, F., L. Alfonso, J. Alcántara, and J. M. Hallen, (2008) "On the Estimation of Failure Rates of Multiple Pipeline Systems", *Journal of Pressure Vessel Technology*, Vol.130.

Carvalho, A.A., Rebello, J.M.A., Souza, M.P.V., Sagrilo, L.V.S. and Soares, S.D.(2008) "Reliability of Non-destructive Test Techniques in the Inspection of Pipelines Used in the Oil Industry", *International Journal of Pressure Vessels and Piping*, Vol.85, 745–751.

Cease, H., Derwent, P.F, Diehl, H.T., Fast, J., Finley, D. (2006) "Measurement of Mechanical Properties of Three Epoxy Adhesives at Cryogenic Temperatures for CCD Construction", Fermi National Accelerator Laboratory, Batavia.

Davies, S.J., Edwards, C., Taylor, G.S. and Palmer, S.B. (1993). "Laser-generated Ultrasound: Its Properties, Mechanisms and Multifarious Applications," *Journal of Physics D: Applied Physics*, Vol. 26, pp. 329-348.

Douglass, C., (2009), Safety Recommendation, National Transportation Safety Board, Pipeline and Hazardous Materials Safety Administration.

El-Shiekh, T. M. (2010). "Leak Detection Methods in Transmission Pipelines." *Energy Sources*, part.A, Vol.32, pp.715–726.

Fuchs, H.V. and Riehle, R. (1991). "Ten Years of Experience with Leak Detection by Acoustic Signal Analysis," *Applied Acoustics*, Vol. 33, pp. 1-19.

Fukuda, T. And Mitsuoka, T. (1986) "Applications of Computer Data Processing and Robotic Technology," *Computers in Industry*, Vol. 7, pp. 5-13.

Gao, Y., Brennan, M.J., Joseph, P.F., Muggleton, J.M. and Hunaidi, O.(2004) "A Model of the Correlation Function of Leak Noise in Buried Plastic Pipes," *Journal of Sound and Vibration*, Vol. 277, pp. 133-148.

Gloria, N.B.S., Areiza, M.C.L., Miranda, I.V.J. and Rebello, J.M.A. (2009). "Development of a Magnetic Sensor for Detection and Sizing of Internal Pipeline Corrosion Defects." *NDT & E International*, Vol. 42, pp. 669–677.

Grabec, I. (1978) "Application of Cross Correlation Techniques for Localization of Acoustic Emission Sources," *Ultrasonics*, Vol. 41, pp. 111-115.

Grabec, I., Kosel, T. And Muzic, P. (1998). "Location of Continuous AE Sources by Sensory Neural Networks," *Ultrasonics*, Vol. 36, pp. 425-530.

Giurgiutiu, V. (2008) *Structural Health Monitoring with Piezoelectric Wafer Active Sensors*, Amsterdam, Academic Press.

Graff, K.F. (1975). *Wave Motion in Elastic Solids*. Dover Publications Inc.

Hatano, H., Chaya, T., Watanabe, S. and Jinbo, K. (1998). "Reciprocity Calibration of Impulse Responses of Acoustic Emission Transducers." *IEEE Transactions on Ultrasonics, Ferroelectrics, and Frequency Control*, Vol.45, No.5, pp.1221–1228.

Hessel, G., Schmitt, W. and Weiss, F.P. (1996) "A Neural-Network Approach for Acoustic Leak Monitoring in Pressurized Plants with Complicated Topologies," *Control Engineering Practice*, Vol. 5, No. 9, pp. 1271-1276.

Hyun, S.Y., Jo, Y.S., Oh, H.C., Kim, S.Y. and Kim, Y.S. (2007) 'The Laboratory Scaled-down Model of a Ground-penetrating Radar for Leak Detection of Water Pipes', *Measurement Science and Technology*, Vol. 18, 2791–2799.

Jiao, J., He, C., Wu, B. And Fei, R. (2004). “A New Technique for Modal Acoustic Emission Pipeline Leak Location with One Sensor,” *Insight*, Vol. 46, No. 7, pp. 392-395.

Kalyanasundaram, P., Jayakumar, T., Raj, B., Murthy, C.R.L., Krishnan, A. (1989), “Acoustic Emission Technique for Leak Detection in an End Shield of a Pressurized Heavy Water Reactor”, *Nuclear Engineering and Design*, Vol.116, pp.181-185.

Kam, S.I., (2010) ‘Mechanistic Modeling of Pipeline Leak Detection at Fixed Inlet Rate’, *Journal of Petroleum Science and Engineering*, Vol. 70, 145–156.

Kholkin A.L., Pertsev N.A., Goltsev A.V. (2008) “Piezoelectricity and Crystal Symmetry” *Piezoelectric and Acoustic Materials for Transducer Applications*, New York, Springer Publishing, pp.17-38.

Kishawy, H.A. and Gabbar, A. (2010). “Review of Pipeline Integrity Management Practices,” *International Journal of Pressure Vessels and Piping*, Vol. 87, pp. 373-380.

Kosel, T., Grabec, I. And Muzic, P. (2000)“Location of Acoustic Emission Sources Generated by Air Flow,” *Ultrasonics*, Vol. 38, pp. 824-826.

Kupperman, D.S., Claytor, T.N. and Groenwald R.(1985) “Acoustic Leak Detection for Reactor Coolant Systems,” *Nuclear Engineering and Design*, Vol. 86, pp. 13-20.

Laodeno, R.N., Nishino, H. And Yoshida, K. (2008). “Characterization of AE Signals Generated by Gas Leak on Pipe with Artificial Defect at Different Wall Thickness,” *Materials Transactions*, Vol. 49, No. 10, pp. 2341-2346.

Lee, Y.C., and Kuo, S.H. (2001). “Miniature Conical Transducer Realized by Excimer Laser Micro-machining Technique,” *Sensors and Actuators A: Physical*, Vol. 93, No. 1, pp. 57-62.

Luo, W. (2005). “Ultrasonic Guided Waves and Wave Scattering in Viscoelastic Coated Hollow Cylinders,” PhD Dissertation, The Pennsylvania State University.

Marin-Franch, P., Martin, T., Tunncliffe, D.L., and Das-Gupta, D.K. (2002). “PTCa/PEKK Piezo-composites for Acoustic Emission Detection,” *Sensors and Actuators A: Physical*, Vol. 99, No. 3, pp. 236-243.

McLaskey,G. and Glaser S.D. (2012). “Acoustic Emission Sensor Calibration for Absolute Source Measurements.” *Journal of Nondestructive Evaluation*, Vol.31, pp. 157–168.

Miller, R.K., Pollock, A.A., Watts, D.J., Carlyle, J.M., Tafure, A.N. and Yezzi, J.J. (1999). “A Reference Standard for the Development of Acoustic Emission Pipeline Leak Detection Technique,” *NDT&E International*, Vol. 32, pp. 1-8.

Muggleton, J.M., Brennan, M.J. and Linford, P.W. (2004). "Axisymmetric Wave Propagation in Fluid Filled Pipes: Wavenumber Measurements in in Vacuo and Buried Pipes," *Journal of Sound and Vibration*, Vol. 270, pp. 171-190.

Muggleton, J.M. and Brennan, M.J. (2004). "Leak Noise Propagation and Attenuation in Submerged Plastic Water Pipes," *Journal of Sound and Vibration*, Vol. 278, pp. 527-537.

Or, S.W., Chan, H.L.W., and Choy, C.L. (2000). "P(VDF-TrFE) Copolymer Acoustic Emission Sensors," *Sensors and Actuators A: Physical*, Vol. 80, No. 3, pp. 237-241.

Ozevin, D. and Harding J. (2012). "Novel Leak Localization in Pressurized Pipeline Networks using Acoustic Emission and Geometric Connectivity," *International Journal of Pressure Vessels and Piping*, Vol. 92, pp. 63-69.

Ozevin, D. and Yalcinkaya, H. (2012). "Reliable Monitoring of Leak in Gas Pipelines using Acoustic Emission Method," CHSM-4, November 5-8, Berlin, Germany.

Pipeline and Hazardous Materials Safety Administration, PHMSA, National All Pipeline Systems: All Reported Incidents Summary Statistics: 1992-2011.

Pipeline and Hazardous Materials Safety Administration, PHMSA, September 28, 2012, Significant Incident Files.

Proctor, T.M. (1982). "An Improved Piezoelectric Acoustic Emission Transducer," *Journal of the Acoustical Society of America*, Vol. 71, pp. 1163-1168.

Proctor, T.M. (1988) "A High Fidelity Piezoelectric Tangential Displacement Transducer for Acoustic Emission," *Journal of Acoustic Emission*, Vol. 7, No.1, pp. 41-48.

Sause, M.G.R., Hamstad, M.A. and Horn, S. (2012). "Finite Element Modeling of Conical Acoustic Emission Sensors and Corresponding Experiments," *Sensors and Actuators A: Physical*, Vol. 184, pp. 64-71.

Stouffs, P., Giot, M. (1992). "Pipeline Leak Detection Based on Mass Balance : Importance of the Packing Term", *Journal of Loss Prevention in the Process Industries*, Vol. 6, No.5, pp. 307–312.

Theobald, P D, Esward, T.J., Dowson, S.P. and Preston R.C., (2005). "Acoustic Emission Transducers-Development of a Facility for Traceable Out-of-Plane Displacement Calibration." *Ultrasonics*, Vol.43, pp. 343-350.

Theobald, P.D. (2009). "Optical Calibration for both Out-of-plane and In-plane displacement sensitivity of Acoustic Emission Sensors," *Ultrasonics*, Vol. 49, pp. 623-627.

Tichy, J., Erhart, J., Kittinger, E., Privratska J., (2010), *Fundamentals of Piezoelectric Sensorics*, Berlin, Springer Publishing.

Wood, B.R.A, and Harris, R.W. (2000). “Structural Integrity and Remnant Life Evaluation of Pressure Equipment from Acoustic Emission Monitoring.” *International Journal of Pressure Vessels and Piping*, Vol. 77, pp. 125–132.

Yaorang, F., Helin L., Pingsheng Z., Baiping D., Baodian M., Zhihao J. (2001). “Failure Analysis and Fitness-for-service Assessment for a Pipeline”, *Engineering Failure Analysis*, Vol.8, pp. 399-407.

Yang, J., Qingxin, Y. and Guanghai, L. (2007). “Leak Identification Method for Buried Gas Pipeline Based on Spatial-Temporal Data Fusion,” *IEEE International Conference on Control and Automation*, Guangzhou, China, pp. 774-777.

VITA

Mr. Hazim Yalcinkaya earned Bachelor of Science in Civil Engineering from Bogazici University with an honors degree in 2011. Mr. Yalcinkaya has been a graduate student at University of Illinois at Chicago since 2011. During the two year study period, Mr. Yalcinkaya completed the National Science Foundation project: “Preventing Imminent Failures of Pipeline Networks via Real Time Damage Detection and Location System.” The project includes the study of variables affecting leak detection on gas pipelines, designing a new shear mode piezoelectric transducer for leak localization applications and introducing a new absolute calibration method for acoustic emission sensors. Mr. Yalcinkaya earned Master of Science degree from University of Illinois at Chicago in 2013.

Publications

Ozevin, D. and Yalcinkaya, H. (2012). “Reliable Monitoring of Leak in Gas Pipelines using Acoustic Emission Method,” CHSM-4, November 5-8, Berlin, Germany.

Yalcinkaya, H. and Ozevin, D. (2013). “Shear-mode Piezoelectric Acoustic Emission Sensor with a Particular Geometry Design,” SPIE Smart Structures/NDE Conference, March 10-15, San Diego, CA.